China Report

SCIENCE AND TECHNOLOGY

No. 117

CHINA REPORT

SCIENCE AND TECHNOLOGY

No. 117

CONTENTS

PHYSICAL SCIENCES

EXPERIMENTS IN PROTECTION AGAINST SHOCK WAVES REPORTED

[Article by Liang Jiongyun [2733 3518 9462]: "Shock Tubes and the Prevention
of Shock Waves; the Importance and the Problem of Protection Against Shock
Waves"]

[Text] The problem of protection against nuclear weapons has been widely stud-
ied in various fields. Every one knows nuclear weapons have four factors that
kill or cause damage: light radiation, shock waves, early nuclear radiation,
and radioactive pollution. Actually, it has also been discovered that the
damage by electromagnetic pulses cannot be ignored either. Among these destruc-
tive, killing and damaging factors, shock waves have the greatest power to
destroy and harm. In the study of protection against nuclear weapons, the
study of protection against shock waves occupies a very important position. The
injury to people inflicted by shock waves includes two types, direct injury and
indirect injury. Direct injury is caused by the effects of shock waves upon
people. Indirect injury is mechanical injury inflicted by the collapse of
buildings and the various objects such as weapons and equipment, sand and stones,
bricks and tiles, and broken glass when shock waves act upon the various build-
ings and objects. Shock wave injuries in a nuclear explosion can be classified
as light injuries, medium severe injuries, heavy injuries and severely heavy
injuries. For each level of shock wave injury inflicted on exposed people on
the ground surface, there is an ultrapressure value of the shock wave, and for
heavy injuries and severely heavy injuries, there are also corresponding dyna-
mic pressure values. In the same ratio of altitude of explosion, the range of
medium shock wave injury inflicted by a 20,000-ton class nuclear weapon exploded
in the air is about 1,000 meters from the point of projection of the center of
explosion on the ground. For the 1 million-ton class device, the range of
medium shock wave injury is 4,000 meters from the point of projection of the
center of explosion on the ground. The range of injury is very large. When
Japan was hit by the atomic bomb, 70 percent of the wounded suffered from shock
wave injuries. When the atomic bomb was dropped on Hiroshima, 60 percent of
the people who died during the early period died from shock wave injuries.

The positive pressure of shock waves from a nuclear explosion lasts for a rela-
tively long time: from 0.3 seconds to 2 to 3 seconds. This enables the shock
wave to enter through various openings into the interior of solid defensive

construction and damage the interior facilities and kill or injure people inside. The problem of how to prevent shock waves from entering through vents, exhaust vents, smoke exhaust vents, water drainage holes, and doors into the interior of defense structures, i.e., the problem of protecting openings, has been given a lot of emphasis by research personnel designing defense structures.

Defense structures are now built underground in order to utilize the supporting capabilities of natural rocks and soil to increase their resistance as the power of nuclear weapons increases. The main part of the command post of the North American Defense Command headquarters has a natural protective layer of 420 meters. In recent years, civilian construction has been emphasized by the nations of the world. Among Europeans, the sayings that "the atomic age is the underground age" and "Europe is going underground" are popular. In Switzerland, 80 percent of the total population is covered. As defense construction goes underground, the problem of propagation of shock waves in rock and soil media has emerged.

Protection against shock waves involves many topics in mechanics, such as the problem of calculating the parameters of shock waves from nuclear explosions, problems of reflection and diffraction of shock waves encountering various types of obstacles, the problem of dynamic load received by buildings and objects on the ground surface, effects of the hot air layer upon shock waves, propagation and attenuation of shock waves entering tube shaped structures and underground tunnels, propagation of the waves in rock and soil media, the problem of the mutual reaction between load and underground structures and media.... In general, there are many problems that have to be studied.

Application of Shock Tube Technology in Defense Tests Against Nuclear Explosions

Research in protection involves a lot of theoretical and computational questions, and experimental research must also be emphasized. From 1945 to 1972, the United States conducted 193 atmospheric nuclear tests, 358 underground nuclear tests and 5 underwater nuclear tests. Nuclear tests were conducted mainly to study the technical problems of nuclear weapons themselves, and at the same time, experiments and tests on the effects of nuclear weapons were also conducted, including experiments on prevention and protection against shock waves. Using nuclear weapons tests to study the problems of prevention and protection against shock waves is the most direct and authentic experiment. But because of the conditions of the nuclear test site, restrictions on personnel participating in the tests due to climatic influences of the various harmful factors, direct experiment cannot completely solve the problem. In seeking economy, reliability and repeatability of the experiments, people have thought of many ways and have developed various kinds of simulated indoor experimental equipment.

Shock tube technology existed as early as the 1880's in the 19th century, but its application in experimental research in the defense against nuclear explosion has a history of only 20 to 30 years. In 1953, Sweden was the first to build a shock tube, with a diamter of 1.0 meters and a length of 11.5 meters. At the end of the 1950's, the U.S. Navy, Army and Air Force built in succession

various types of shock tubes. The large conical shock tube built by the U.S. Naval Weapons Laboratory was the largest: the tip of the cone had a diameter of 0.4 meter, the bottom of the cone a diameter of 7.2 meters, and the total length was 736.4 meters. Our nation's research in the use of the shock tube in the defense against nuclear explosion began at the beginning of the 1960's when the shock tube was used in studying defense against nuclear explosion. What kinds of experimental research in the problem of prevention and protection against shock waves can the shock tube be used for?

I. Experimental Research in Shock Waves Entering Tube Structures, Underground Tunnels and Various Types of Exits and Entrances

When a shock wave enters a tube structure or an underground tunnel, the intensity of the new shock wave formed inside the structure or tunnel varies according to the different angles between the direction of the incident wave and the axial direction of the tube structure or underground tunnel. As the shock wave propagates inside the tube structure, the intensity of the shock wave weakens because of the effects of the layer against the surface and expansion waves. By varying the section of the tube or the direction of the axial line, the intensity of the shock wave may lessen or may increase. If the area of the tube shrinks, the intensity of the shock wave will increase. If the tube is not straight, reflection and refraction will occur during the course of propagation of the shock wave, and the ultrapressure value will increase. The increase in ultrapressure value caused by the geometric shape of the tube is always smaller than the ultrapressure value of positive incidence and reflection of the shock wave. When a shock wave propagates in an uneven section or curved tube, the image of movement of the wave system is more complex; using wave motion theory to calculate it is complicated and unnecessary in practice. The empirical and quasi-empirical computational formulas proposed abroad are mainly summarized from experiments. The U.S. Air Force Design Manual clearly points out that the main source of information is the study of the shock tube in a model underground tunnel system. Domestically, "experimental study of the shapes of exits and entrances of several types of underground tunnels" and "experiments in the pressure distribution at exits and entrances of civil defense works" were carried out, and through shock tube experiments, we obtained the pressure distribution for various shapes of exits and entrances and pressure values on doors, and as long as we follow conditions similar to Cp = 1, Cp = C_T in designing the model, the results obtained can be used. If they can be checked and revised against the experimental results of nuclear effects, they will be more reliable when they are actually applied.

II. Experimental Study of the Dynamic Load of Ground Surface Structures

The dynamic load on structures is not only related to the parameters of the free field of the incident shock wave (wind velocity, pressure, direction), it is also related to the shape of the structures and the surface properties. In general, dynamic load is determined by multiplying dynamic pressure by the coefficient of resistance. The coefficient of resistance is needed not only in designs to resist explosions, but also in aviation and aircraft design. But the coefficient of resistance measured in the constant velocity wind tunnel cannot be directly used for ground surface structures to resist explosions

3

because the wind velocity following the shock wave varies instantaneously. The effect of parameters of the free field upon resistance is represented by the Reynold's number R and the Mach number M. The Reynold's number concerns regulation of the form oi activity of air flow around objects; a low Reynold's number indicates a flat and smooth laminar flow, while a high Reyrold's number indicates the formation of turbulent trail flow behind a structure, and the border layer of turbulent flow will transmit the smaller resistance to the target. Within the range of the critical Reynold's number, air flow is unstable, and it varies with time. The Mach number can be divided into three ranges: The subsonic range is about M < 0.5, the air flow around structures is subsonic. The transonic range is 0.5 < M < 2, air flow around structures is subsonic and ultrasonic. The ultrasonic range is about M > 2, air flow around structures is all ultrasonic. To study the dynamic load of ground surface structures, experiments to test the roof boards of attached type civil defense work and destruction of ground surface structures using the shock tube in the defense against explosions, experiments of load distribution on cones and studies of the effects of topography on shock waves have been conducted domestically.

III. Experiment on a Structure Built for Defense Against Explosions

Experiments on structures constructed for defense against explosions involve many aspects. Many experiments have been conducted both domestically and abroad. They can generally be classified into two main categories. One is facilities to resist waves from explosions, such as removable doors to resist waves from explosions, protective and defensive doors, wave absorbing troughs, and filtering facilities. The other is protective and defensive structures, mostly shallowly buried structures, such as beams, arcs and round structures. Experiments on facilities to resist waves from explosions mostly involve testing the strength of the facilities and the performance in the defense against waves from explosions to see whether they satisfy the standards and demands of design. Experiments in defense and protective structures are often small-scale experiments because similar conditions are difficult to duplicate completely, and they are used to test the theoretical and computational methods and to explore the patterns of dynamic effects of the structures. A lot of experimental research on these two categories of problems to resist explosions utilizing the shock tube has been conducted domestically. In small-scale experiments on shallowly covered structures, problems in two aspects must be considered. The first is that the position of the structure must assure that shortly after the peak value of the compression wave passes the structure, i.e., before the largest shift of the structure occurs, the reflected wave of the front wall of the box shaped structure and the free waves behind the box shaped structure cannot reach the structure. The second is the problem of analysis of the measured results of the deformation parameters of the structure. The measured parameters must be simultaneously recorded as to their starting time to facilitate reading the parametric values of each point at a certain instantaneous time. The analysis should emphasize the reaction of the structure at the time the largest peak value of the compression wave passes through the entire structure, or the instantaneous situation at the time of occurrence of the largest value of shift of the structure. Analysis of the entire waveform cannot be done because the

entire waveform includes reflection by the side walls and the effects of free waves. To study the effects of the side walls of the box shaped structure, optical photographs (coronagraphic measurements) were taken of the image of wave motion of the box shaped structure encountering air shock waves incident upon a simulated box structure. The experiments showed that positions of the box shaped structures that satisfy the demands of the experiment can be selected. Some comrades doubted whether the shock tube could be used in the experiment of shallowly covered waveform and the effects of reflection by the side walls. They did not realize that the use of the shock tube in the experiment on aerodynamic models frequently utilizes the period of stable and constant flow for the experiment. Testing box shaped structures of sand as the medium showed that the range of the effect of reflection of the bottom of the box shaped structure is not large, and if an energy absorbing pad is used, the effects of reflection of the bottom of the box shaped structure can be further reduced. This shows that the use of the shock tube in the experiment of shallowly covered small structures is feasible.

IV. Experiment on the Soil's Dynamic Properties and Propagation of Stress Waves in the Soil

Because the shock waves produced in the shock tube are a strong interrupted surface, they have a sudden loading form, the speed of which is very high, and they are better for testing the dynamic properties of the soil. To increase the peak value of pressure, frequently end surface reflection is used to carry out the experiment. The shock wave produced by the even section shock tube is a one-dimensional wave. A cylindrical piece of soil is connected to the end of the tube for the experiment, and as long as the effects of side wall friction are eliminated, experimental research on the propagation of a one dimensional wave in the soil can be carried out. Abroad, experiments on soil dynamic properties and propagation experiments of stress waves in soil are mostly carried out in a vertical shock tube. The vertical shock tube of the Atomic Weapons Research Center of Great Britain has a diameter of 0.61 meters and a height of 16 meters; the box at the lower end is 3 x 3 x 1.6 meters, the reflection pressure is 28 kilograms/cm^2, and the period of the effect is 24 millimeters.

V. Experiments on the Biological Effects of Shock Wave Injury

Since the emergence of nuclear weapons, "shock wave injury" has become an important research topic in defense medical science. Domestic and foreign materials show that study of the source of infliction of "shock wave injuries" is mostly carried out using the shock tube. Shock tube experiments on biological effects can be qualitatively observed and also quantitatively measured, and they can be used in the systematic study of early diagnosis of shock wave injuries, pathological anatomy and experimental treatment. Indoor experiments can be repeated to facilitate observation; personnel participating in the experiment can carry out experimental research work without protective measures. This is favorable to the systematic study of things that follow a logical pattern. But the efforts must be combined with experiments on nuclear effects to find the differences and the related factors between the two before the similarity of the indoor experimental results can be judged.

VI. Inspection of the Dynamic Properties of the Pressure Sensor

Inspection of the dynamic properties of the pressure sensor mainly includes examination of the standardized curve of the pressure values, frequency characteristics and damping characteristics. Experimental equipment has been developed to study and examine the dynamic properties of the pressure sensor; the shock tube is one such piece of equipment, and it is effective. The shock tube can produce a strong section, and this assures a steep pressure front so that the signal has the characteristic of a step signal. There is a stable and constant flow zone behind the shock wave, followed by an unstable and nonconstant flow. The entire duration can reach 110 ms (experimental data of the ϕ160 shock tube of our department). The pressure waveform produced by the shock tube has a rather wide frequency band. It is more ideal equipment for examining the dynamic properties of the pressure sensor. The pressure value can be converted using the Mach number of the shock wave. A more reliable standard value of pressure can be obtained using a measuring system to measure the velocity of the shock wave in combination with a highly precise instantaneous numerical value voltmeter. Large numbers of pressure standardization experiments show that using the shock tube to standardize ultrapressure sensors is accurate and reliable: the relative error is within ±2 percent. In studying the question of inspecting the performance of dynamic pressure sensors, experiments show that the diffraction characteristics, damping characteristics and drag characteristics can be analyzed from the response curve of the sensor. In studying the question of standardization of dynamic pressure values, because they are inside the specific constant flow area, the velocity of the air flow in front of and behind the contact surface is the same, but the density is not the same, and the dynamic pressure values are also different, manifesting a step form. The experimental and theoretical values of dynamic pressure frequently deviate from each other when the ultrapressure value is large. In using the shock tube as the standardization equipment for dynamic pressure, further studies in the conversion of numerical values and error analysis are needed.

In summary, the uses of the shock tube are broad and it is an indispensable piece of equipment in experimental study of defense against explosions. As add-on equipment, the technology is more mature. But how to utilize this type of equipment to more effectively carry out various experiments on structures to defend against explosions still requires further study of the theory and techniques of the experiments; for example, the similarity problem in the experiment on structures to defend against explosions, reduction of wall friction of the box shaped structure, technical measures of reflection by the wall of the box shaped structure, measures to increase pressure, and error analysis in high pressure standardization. In general, any kind of experiment must be based on the demands of the experiment and the properties of the equipment to carry out a good design for the plan of the experiment. Sometimes, certain improvements in the original equipment are required based on the demands of the experiment. Experimental equipment can only provide experimental conditions for definite properties and how to utilize these conditions to solve one's own research problems also involves the question of studying related technology.

ARTICLE DISCUSSES PROBLEM OF PLASMA IN HIGH VELOCITY FLIGHT

[Article by Wu Chengkang [0702 2110 1660] et al* of the Mechanics Institute of the Chinese Academy of Sciences: "Problems Related to Plasma in High Velocity Flight"]

[Text]   When a long range ballistic guided missile and an artificial satellite, a space vehicle or a planetary explorer enter the atmosphere, because of the high velocity of flight, the surrounding air is heated to a high degree, forming a partially ionized plasma, and greatly affecting the structural reliability and heat conduction of the vehicle in flight, radio communications, and the physical phenomena during flight. High performance space vehicles require a propulsion system that will last a long time, that has a small thrust and a very high specific impulse. For this, new electrical propulsion methods such as electrothermal propulsion, ion propulsion and plasma propulsion have been developed. This article will briefly discuss three aspects: high temperature heat conduction of the plasma in high velocity flight, the effect of the plasma sheath upon electromagnetic waves in high velocity flight, and the high specific impulse electrical propulsion method.

I.   High Temperature Heat Conduction of Plasma in High Velocity Flight

1.   The heat environment. When a high velocity flying vehicle enters the atmosphere, the air in front is violently compressed by the flying vehicle, a strong friction between the surrounding air and the wall surface of the flying vehicle occurs, and the atmospheric temperature rises to 7,000, 8,000 or even over 10,000 degrees, forming a partially ionized plasma. For different flying vehicles, the parameters of the plasma produced by the different shapes, velocity, height and orbital time of the flying vehicle will be different and the environment of heating of the flying vehicle will also be vastly different. Basically, the heat environments of the high performance guided missile and manned space vehicle are of two different types.

A transcontinental guided missile has a small nose, a long body and large angle reentry capability for low resistance to hasten attack and improve precision. Within 20 to 30 seconds, it can drop to an altitude of a dozen or so kilometers while the velocity is still over 5 kilometers/second. The characteristics of plasma are high pressure and high temperature. The plasma belongs to a continuous medium, and the plasma is in or approaches thermal equilibrium. The heating of the flying vehicle is mainly due to convective heating, the heat flow is large, the shear is strong, and the time is short.

The winged gliding type aircraft is required to carry people and make many flights; therefore it uses small angle reentry and reduces flying speed at a high altitude over a long period. Therefore, the characteristics of the plasma are low pressure, high temperature, nonequilibrium, and it belongs to a transient area between a free molecular flow medium and a continuous medium. Heating of the flying vehicle is mainly convective heating, the heat flow is small, shear is weak, and the time is long.

During reentry of the trajectory satellite, the plasma is between the two described above but closer to the latter, especially a manned space vehicle. The Apollo spaceship that returned from the moon to earth had a higher velocity, and the radiative part of the heating cannot be neglected.

Probes sent into the planetary atmosphere have an extremely high velocity, the temperature of the plasma produced is also high, the heating of the vehicle is mainly due to radiation, and convection is also important. The actual parameters and the characteristics are determined by the atmospheric composition of the planets and the parameters, mass of the planets and the flight orbit parameters.

In the problem of heating of the plasma in high velocity flight, the representative parameters are the air parameters h_s, T_s, p_s (enthalpy, temperature, pressure intensity) of the fore stagnation point of the flying vehicle, the heating rate q_s, q_{max} (stagnation point and largest heat flow) of the flying vehicle and the shear stress τ_{max} (maximum shear stress). The parameters of the typical orbit and the air flow at the stagnation point of some high velocity flying vehicles at the time of entering the atmosphere are shown in Figures 1-4.

The heating of a surface by air is greatly affected by the roughness of the wall surface, materials that have entered into the air layer against the surface, the presence of solid particles in the flow field, and changing of laminar flow into turbulent flow. In radiative heating, the air's radiative properties, absorption of solids and reflective characteristics are all very important. These problems are also subjects of study now.

2. Heat prevention measures. Because of aerodynamic heating, it is necessary to take measures to prevent heating. Many methods to prevent heating have been proposed and tested, such as the metallic heat sink, radiative scattering of heat, prevention of heating by erosion, sweating and cooling, and even the utilization of magnetic fields to cause the plasma to deviate from the surface of the object. But after many years of practice, the most mature measure to
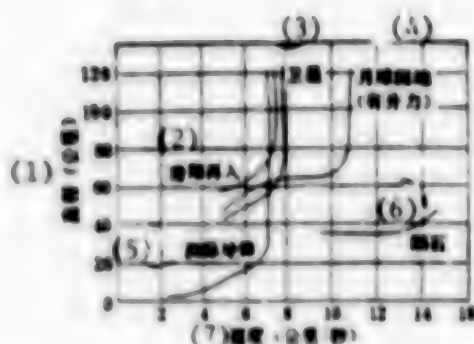
Figure 1.   Typical Orbits of Several
             Types of Reentry Space
             Vehicles

Key:
(1) Altitude (kilometers)
(2) Gliding reentry
(3) Satellite
(4) Returning to earth from
     the moon (with lift)
(5) Intercontinental guided missiles
(6) Meteor
(7) Velocity (kilometers/second)
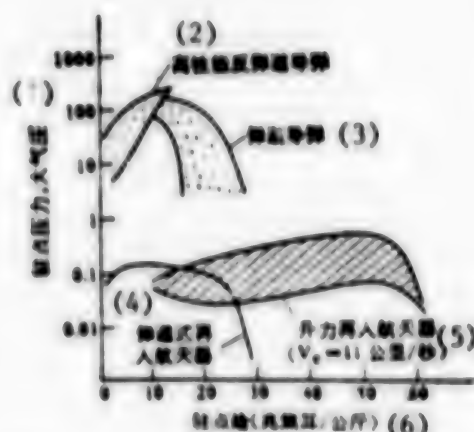
Figure 2.   Typical Stagnation Point
             Parameters of Several Types
             of Reentry Space Vehicles

Key:
(1) Pressure at stagnation point,
     atmospheric pressure
(2) High performance anti-ballistic
     missile
(3) Ballistic missile
(4) Ballistic reentry space vehicles
(5) Lift reentry space vehicles
     (V_e = 11 kilometers/second)
(6) Enthalpy at stagnation point
     (mega jules/kilogram)

prevent heating under a high temperature heat flow at present is the erosion
method. In low temperature heat flow, the erosion-radiation method can be used.
The sweating and cooling method has always remained in the research stage. The
magnetic field method has only been explored in principle; because it is diffi-
cult to materialize, no further work has been done in this regard.

The two different types of heating environments require different heating pre-
vention systems. Prevention of heating for guided missiles is mainly by ero-
sion. Heat prevention for space vehicles is mainly by insulation. But for each
flying vessel, for each part, because of the different heating environments and
functional demands, the heating prevention system used always involves detailed
work, and new materials, technologies and structures are continually being
developed to adapt to the various demands.

3. Calculation and simulation experiments of heating prevention by erosion.
Theoretical analysis and computation, ground simulation experiments and flight
tests are the three main ways to solve the problem of aerodynamic heating in
high velocity flight. They are complementary and mutually supplementary. After
a lot of research work, heat conduction on the wall surface in high temperature
air flow and the erosion process of erosive materials are in principle under-
stood and they can be calculated. The content of the calculations include

9
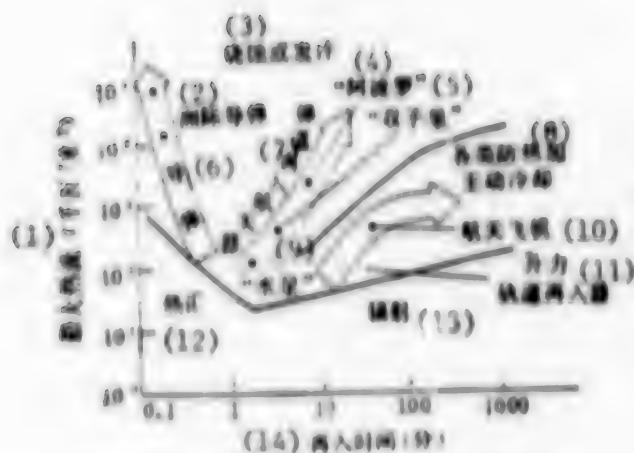
Figure 3. Reentry Time and Maximum Heat
Flow of Several Types of
Reentry Space Vehicles

Figure 4. Environmental Parameters
at the Stagnation Point
of the Space Vehicle
Entering the Atmosphere
of Jupiter

Key:
(1)   Maximum heat flow (kilowatt/meter^2)
(2)   Intercontinental guided missile
(3)   Erosion or sweating
(4)   "Apollo"
(5)   "Gemini"
(6)   Guided missile
(7)   Ballistic reentry space vehicle
(8)   Various types of prevention of
      heating plus initiative cooling
(9)   "Mercury"
(10) Space flight craft
(11) Lift orbital reentry vehicle
(12) Heat sink
(13) Radiation
(14) Time of reentry (minutes)

Key:
(1)   Megapascal (mega neutrons/
      meter P_a)
(2)   Megajules/kilogram
(3)   Heat flow, kilowatts/cm^2
(4) V_E = 48 kilometers/second
(5)   Time (second)

chemical reactions, calculation of the high temperature air flow layer against
the surface with injected mass, internal heat conduction and chemical changes
in solid materials, production of decomposed gases and the flow through solids,
melting of wall surface materials, flow and evaporation processes. The details
of these processes have been extensively studied abroad, complex computational
procedures have been compiled, and the results of ordinary situations can be cal-
culated. But there are still complex situations such as the formation of grooves
and patterns on surfaces, mechanical erosion of solids, partially complex shapes,
new materials, and the erosion mechanism which are not understood yet and
physical data that make it difficult to carry out accurate computations. The
more mature method of calculation also needs to be proven by experiment. The
production techniques and structure must also be examined and tested. There-
fore, simulation experiments are an important means to study heating and pre-
vention of heating in high velocity flight.

For problems of heating in high velocity flight, completely duplicating in-flight conditions or creating completely similar experimental conditions are impossible. We can only use approximate or partially similar experiments to combine experimental results and theoretical analysis, to combine the experimental results of each part to solve the problem. To study the phenomena in fluid dynamics, we can use low temperature materials for experiments in the wind tunnel. To study heat conduction in high temperature air flow, we can use shock wave wind tunnel experiments. But to test the materials and structures to be actually used for high temperature heating prevention, there must be a high temperature air flow of long duration (counted in seconds or minutes). Of these methods, the generation of plasma by electric arc heating and the combustion air flow experimental equipment are two types that are used the most. The combustion air flow experimental equipment is mainly used to test structures of large dimensions and to study changes in the external shape, but this method's air flow temperature is still far lower than the actual temperature. The only continuous experimental equipment that can truly produce an air temperature close to the actual air temperature in flight is the electric air heater.

Beginning from the end of the 1950's, electric arc heating of air flow has been used to study the heating problem in high velocity flight. Various forms of the heater have been tested over many years. Figure 5 shows only a small number of them. Many types of electromagnetic accelerators were also tested. Lorentz force that utilizes the functions of the magnetic field and electrical currents was used to produce high velocity and high enthalpy air flow. But after 20 years of development, high enthalpy equipment used as equipment for aerodynamic heat simulation experiments gradually centered around large power, direct current and long arc type heaters. Electromagnetic accelerators did not develop further because of their own complexity and the experimental trend of combining partial experiments and theoretical analysis and computations.

The common used small power heaters of lower enthalpy values are generally spray gun types. But a serialized and mature design to assure stability of the parameters, long life of the electrodes, less pollution, and adaptability to the range of the various working gases and the various operating parameters is still lacking, and this is especially true domestically. For large power heaters, because of the series of problems caused by large electrical currents, the complexity of parallel heaters, and the shortcomings of the alternating heater in maintaining the range of stability of the electric arc and parameters, the present trend is to use single unit direct current heaters of high electrical voltage (reaching 50,000 volts) and medium electrical current ($\leqslant$ 2000 amperes). At the end of the 1960's, the types of heaters developed toward the high voltage, medium enthalpy and large current stable long arc with circulated air as well as the low voltage, high enthalpy and small current stable long arc of folded plate walls, but they all have functional shortcomings. During the 1970's, a heater combining these two methods was developed, i.e., thicker folded plates were used to retain the arc length and circulated air was injected between the plates to prevent mix up of the arcs. Based on the demands of simulation of different heat environments, the experimental method can be varied, such as the use of subsonic jets, supersonic jets, shielding, and supersonic wind tunnels. Recently, because of the need for the Jupiter probe to enter the atmosphere of Jupiter, the model was placed in the arc column part of the long arc to utilize high temperature radiation to conduct heat in the experiment.

11
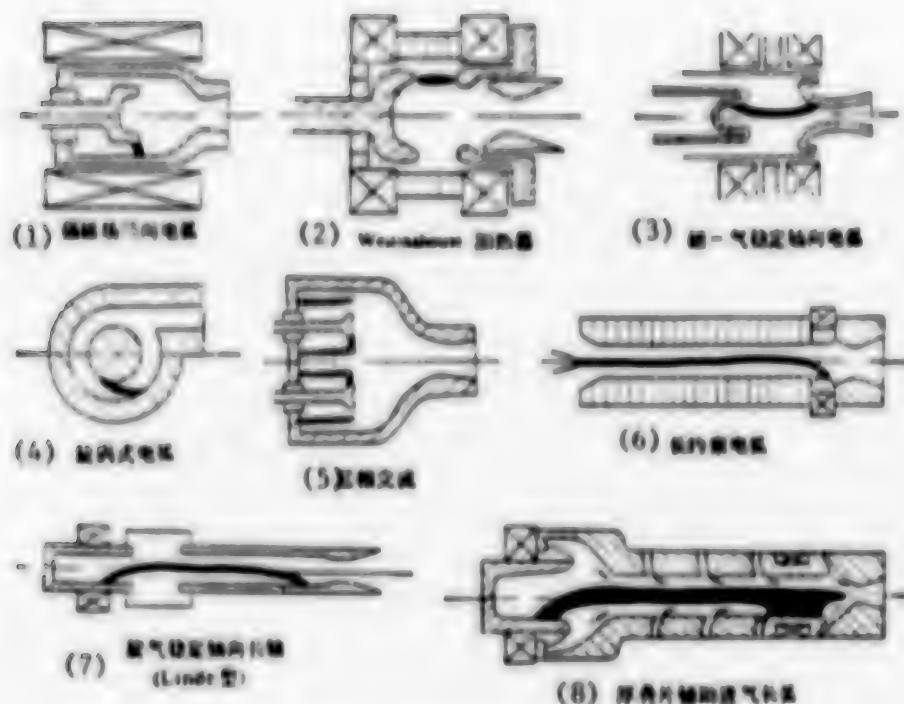
Figure 5. Various Forms of Electric Arc Heater

Key:
(1) Strong magnetic field radial electric arc
(2) Westinghouse heater
(3) Magnetic--air stable axial electric arc
(4) Eddy electric arc
(5) Triple phase alternate flow
(6) Long-bounded electric arc
(7) Lind type circulated air stable axial long axis
(8) Thick folded plate auxiliary injected air long arc

Calculation of the performance of the electric arc heater has produced rela-
tively good results for the long arc wall stable type, but for other types of
heaters that are more complex, direct calculations are still immature. Using
the principle of similarity, we can extrapolate the performance of certain
similar types of heaters, but the degree of success also varies.

4. Brief summary. Generally, the technical problems in aerodynamic heating
of guided missiles and spaceships entering the atmosphere have already been
solved abroad, but high performance missile heads, new materials and more de-
tailed mechanisms, more reliable methods of simulation experiments and problems
of entering the atmosphere of planets are still subjects of study. The scope
of research work being launched now is not as wide as before, but profound and
improved work is still being carried out.

II. The Problem of the Plasma Sheath in High Velocity Flight

1. The nature of the problem and the parameter of the plasma sheath. The
so-called plasma sheath refers to the high temperature ionized body of air
produced in high velocity flight, especially the free electrons, which forms
an envelope over the exterior of the flying vehicle. It hinders radio communi-
cations, and at the same time, it produces an electrically charged tail behind
the flying vehicle which can be detected by radar waves. The plasma sheath
causes serious attenuation or interruption of the transmission of electromagne-
tic waves between the flying vehicle and t'æ outside world. Thus, the verbal
communications of manned spaceships, real time remote measurements of the
parameters of the flying vehicle, final control and guidance of guided missiles
and electronic jamming cannot be carried out normally, and this frequently
occurs at the critical moment during the course of the flight. Certain charac-
teristics of the flying vehicle can be recognized from the scattering of the
radar wave caused by the electrically charged tail, so this problem has special
meaning in tracking and identification of flying objects. To improve communi-
cation with the outside, the problem of transmitting electromagnetic waves
through the plasma sheath needs to be solved. To utilize the electrical char-
acteristics of the tail for defense against sudden attacks or anti-ambush defense
requires a clear understanding of the characteristics of the tail and the factors
that affect these characteristics.

The parameters of the plasma sheath are mainly the distribution of electron den-
sity, followed by the frequency of collision of electrons and electron tempera-
ture. These are mainly determined by the altitude, velocity of the flight and
the material shape of the object in flight. In the case of a large blunt nosed
flying object (such as the Apollo manned spaceship), the ionization of air is
mainly produced at the head where there are strong shock waves and nonviscous
flow. After expansion, the ionized air flows to the field of flow in the back
part of the flying object. In the case of a flying object with a pointed nose
and a thin long body, electrons mainly occur in the layer against the surface of
the object. For a small blunt nosed flying object with a thin long body, the
contribution of the two are different at different flying altitudes (Reynold's
number). At a high Reynold's number, the electrons mainly come from the entropy
layer; at a medium Reynold's number (over 40 kilometers), the contribution by
the layer against the surface of the object and the entropy layer is similar.
At a low Reynold's number (over 70 kilometers), the viscous effect spreads
through the entire shock wave layer. As the altitude varies, chemical reac-
tions also change from equilibrium to nonequilibrium and freeze the motion of
flow. The distribution of the parameters of a typical plasma sheath is shown
in Figure 6. Besides the flight parameters, the materials spewed from the sur-
face such as products of erosion or electron absorbing materials produce a visi-
ble effect upon the ionization energy; for example, materials containing potas-
sium and sodium increase electrons, materials containing fluorine reduce
electrons.

The calculation of the parameters of the plasma sheath mainly involves calculat-
ing the various types of chemical reactions together, including ionization
reactions in the flow field, i.e., the variation of the composition of the gases
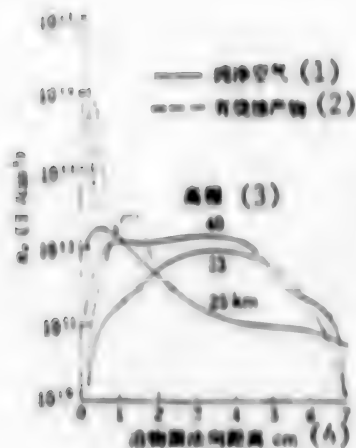
Figure 6. Electron Density Distribution on the Side of the RAM-C Warhead

Key:
(1) Pure air
(2) Erosive products present
(3) Altitude
(4) Distance along normal direction of surface of object

along with changes in the flow field. Under large Reynold's numbers, the flow tube method can be used. It is based on the distribution of pressure of a known nonviscous flow field and it uses the one dimensional flow in the flow tube to specifically study the effects of chemical reactions. There are also several methods to calculate the layer against the surface of objects. For medium and small Reynold's numbers ($Re_e > 10^2$, equivalent to an altitude of 80 to 30 kilometers), the simplified Navier-Stokes equation is used to solve the flow field. For small Reynold's numbers, the method of directly solving the N-S equation must be used. In theoretical analysis, the effects of the separation of the flow field and the vortex upon electron density, the effects of erosion products, and the effects of jet materials upon the electrons still need to be studied, as well as the effects of chemical reaction constants.

In-flight measurement of the parameters of the plasma sheath abroad has involved the use of the waveguide antenna, static probe, radio frequency and electrical conductivity probe, electro-acoustic probe, resistance line probe, microwave radiation counter, and separated notch antenna. At present, the method of measurement is still in the developmental stage. A lot of work should also be done to study the sensor principle, confirm the measurements in the laboratory, to analyze data, to study convenience and reliability of sensors carried by missiles, and to study ways to lower the manufacturing cost.

2. The effect of the plasma sheath upon electromagnetic waves. The propagation of electromagnetic waves in an uneven and bounded plasma is complex. To qualitatively analyze the phenomena occurring on the flying object, we consider the situation of an electromagnetic wave passing through a layer of even plasma (one dimensional propagation) of known thickness and infinite section. According to approximation analysis, we know that the relationship between the frequency

ω of the electromagnetic wave and the frequency ω_p of the plasma is critical. $\omega_p = \sqrt{n_e e^2/\varepsilon_0 m_e}$, where n_e is the electron density, e and m_e are the electron charge and mass of the electron, ε_0 is the dielectric constant of vacuum. In the simple case in which the electron does not collide with other particles, we can conclude that when $\omega \gg \omega_p$, the electromagnetic wave can pass through the plasma without attenuation. When $\omega \ll \omega_p$, the electromagnetic wave propagating inside the plasma attenuates while the electromagnetic wave propagating from the outside toward the plasma will be completely reflected by the boundary surface. For a plasma will be completely reflected by the boundary surface. For a plasma with collision, the situation is more complex. But for a relatively low collision frequency ($\nu \ll \omega_p$), the difference between this situation and that without collision is not very great.

We can obtain the parameters of the plasma from the effects of the plasma sheath upon the electromagnetic wave. Therefore the attenuation and phase shift of the electromagnetic wave can be used to measure the parameters of the plasma; this is also called "plasma diagnosis."

3. The way to solve the problem of hindrance to communications caused by the plasma sheath. Various measures such as increasing power and adding a magnetic field have been tested, but the more hopeful method is to increase the frequency of the electromagnetic wave and the discharge of electron attracting materials so as to reduce the electron density of a part of the plasma sheath.

It can be seen from the relationship between ω_p and n_e that the plasma frequency corresponding to the electron density of $n_e \approx 10^{12}/cm^3$ is 10 GHz. If the communications frequency used is higher than 10 GHz, i.e., millimeter waves, then the general problem of the plasma sheath of the antenna position of ballistic missiles can be solved. The frequency of millimeter waves is higher than that of the present day ordinary communications systems but technically this can be completely realized.

The reason for discharging electron attracting materials is to cause the electrons and the electron attracting materials to form negative ions, thus reducing the density of free electrons, and also reducing the frequency of the plasma so that the communications frequency becomes higher than ω_p and the attenuation of electromagnetic waves in transmission is lessened.

The most effective electron attracting substance is a liquid. Spewing it from the upper reaches of the antenna into the field of flow can reach a definite depth of penetration, and because the velocity is lower than the gases in the field of flow, it can remain in the field of flow for a relatively longer period. In the field of flow, because of aerodynamic bursting (low altitude) and bursting by evaporation (high altitude), large amounts of fine liquid droplets are produced, becoming the third bodies for the electrons and ions to combine on their surface. Overly abundant electrons will cause some of the molecules on the surface of the liquid droplets to convert to negative ions; the latent heat of evaporation of negative ions is lower than neutral molecules, so the liquid droplets can evaporate more easily. Thus, the liquid mist can

effectively adsorb electrons, and the electron density of the local area can be reduced. In addition, when a liquid evaporates, it absorbs heat and the local temperature drops. This will also reduce the electron density and benefit the propagation of electromagnetic waves.

The method of discharge and t   quantity are key problems. How to use the least amount of discharged substance to obtain the best improvement in the results of communications is a problem worth studying.

In the ground surface experiments and research in the plasma sheath, the electric arc heating wind tunnel can be used, or a plasma can be generated by a plasma generator in an ordinary wind tunnel. The ballistic target is very suitable for studying the ionized tail. In ground surface experiments, the electrical probe is a simple and reliable probing instrument. Microwave measurements can provide some parameters of the plasma, but to obtain detailed distribution of the parameters, the microwave equipment needed is very complex.

Because of the limitations of ground surface experiments to simulate the plasma sheath, true quantitative experiments frequently have to rely on in-flight experiments to complete. The main plasma sheath in-flight experiment, RAM project, made public by the United States, was carried out from 1961 to 1970 in three series (A, B, C) involving a total of eight launches. Except for the first launch, which was a failure, data on the plasma sheath gathered by the various probing instruments were obtained. The Trailblazer Project was carried out in two stages from 1966 to 1973 involving a total of nine launches. The degree of emphasis on the plasma sheath problem abroad can thus be seen.

4. Brief summary. The problem of the plasma sheath is one of the key problems in guided missiles and space technology. After over 10 years of active research abroad, some problems are in principle understood, but many details still require continued research. The actual method of solving the problem may have been found but the application plan is still kept secret.

III. The Problem of Electrical Propulsion in Space

Beginning from the 1950's, foreign nations have carried out a lot of profound studies in electrical propulsion. Over 10 different types of electrical thrusters have been developed at different times, and several of them have already been successfully used in space. International conferences are continuously being held. The electrical thruster has a high specific impulse, small thrust, long life, high precision and reliability. It will be applied in the positional control of various types of satellites, space stations and space probes, positional maintenance and orbital corrections, and main propulsion systems in future planetary space flight. The basic principle of electrical propulsion is the utilization of various kinds of electrical and magnetic effects to accelerate the propulsive working mass to a jet velocity far beyond the jet speed which the combustion of chemical fuel can reach, and thus an extremely high specific impulse is obtained--the impulse (product of thrust and function time) of the flying object produced by each kilogram of working materials jettisoned. At present, the successfully developed electrical propulsion systems can be divided into three main types: electrothermal, static, and electromagnetic. These three types of electrical propulsions are separately introduced below.

1. Electrothermal propulsion. Electrothermal propulsion is a simple improvement over the cold air thruster. It utilizes resistors or electric arc discharge as the heat source to increase the enthalpy value of the working mass and thus increases the velocity of the exhaust. There are two types: the stable type and the pulse type. The working mass can be hydrogen, nitrogen, ammonia, or hydrazine. Early research used the electric arc to heat the working mass; reaching a higher specific impulse, hydrogen was used as the working mass, but true in-flight experiment was not realized. The resistor heating type thruster has been used in satellites. In 1968, the resistor heating ammonia thruster operated on the satellite, giving a thrust of 222 millinewtons, a specific impulse of 135 seconds, and power of 11 watts. It was used for positional control of the satellite. It can be seen that this type of propulsion does not have a very high specific impulse (of course higher than cold air), but it is convenient to use. In recent years, there have been more studies of electrically heated hydrazine propulsion. This type of thruster uses electrical heating to reach a temperature for hydrazine to decompose chemically, increase reliability, and increase the specific impulse. Performance reached a thrust of 320 millinewtons, a vacuum specific impulse of 320 seconds, a life of 100 hours. Plans call for the use of an electrically heated hydrazine thruster to maintain the northern and southern positions of the communications satellite. The main advantage of the electrically heated thruster is that its structure is simple, it is versatile and it can operate by impulse. Its shortcoming is that the temperature it can reach is limited, the exhaust velocity is less than 10^4 meters/second, the life is not long enough.

2. The static thruster. The static thruster utilizes the electrical field to accelerate ions, thus producing thrust. Its main components are the ion generator, the acceleration electrical field and the accelerated electron neutralizer. The working mass (liquid cesium or mercury, inert gases can also be used) in the ion generator flows through a supply system and evaporates in an evaporator, then it enters into a discharge chamber. Inside the cylindrical discharge chamber, the electrons emitted from the cathode undergo a spiral motion about the lines of magnetic force under the action of the radial electric field and the longitudinal magnetic field. They collide with the atoms of the working mass to form ions. Downstream of the discharge chamber is a screen grid having the same electrical potential as that of the main cathode. The acceleration pole is less than 1 millimeter downstream from the screen grid, its electrical potential is negative, forcing the ions to jettison out at accelerated velocity. At the exit is a neutralizer that gives the jettisoned electron jet electrical neutrality. The principle of the static thruster is shown in Figure 7. At present, the United States NASA is concentrating efforts on the development of the main thruster for use in φ30 cm planetary flight and orbital lifting and the thruster for maintaining the southern and northern positions of the φ8 cm synchronous satellite. The φ30 cm thruster has a thrust of 135 millinewtons, a specific impulse of 3,000 seconds, and total power of 2,700 watts. The φ8 cm thruster has a thrust of 10 millinewtons, a specific impulse of 3,000 seconds. The life required is over 20,000 hours. It can be seen that the ion thruster is a true high specific impulse thruster.

The static thruster has been tested and studied for many years, including durability tests in space, but at present it is still in the stage of prototype
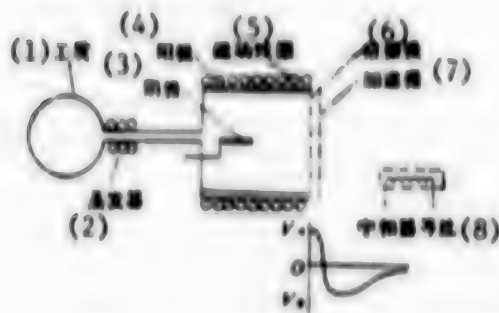
Figure 7. Illustration of the Principle of the Electron Blast Type Static Thruster

Key:
(1) Working mass
(2) Evaporator
(3) Cathode
(4) Anode
(5) Magnetic coils
(6) Screen grid
(7) Accelerator grid
(8) Neutralizer filament

experiments. Task analysis has been conducted for the electrical propulsion system for space flights in the solar system. In addition, in recent years, efforts to explore the applicability of the principles and technology of the ion thruster in industry have emerged. For example, people have proposed the use of splash sedimentation, ion beam processing, surface treatment involved in the ion thruster to provide new technologies, new instruments and new materials for industry, biology, medical sciences and material science. This is a new trend worth noting. This also shows that for a new technology to have a strong life force, its application in many aspects must be sought.

3. Electromagnetic thruster. The electromagnetic thruster utilizes the effects of electromagnetic force to accelerate the plasma jet to produce thrust. There are three types: the stable type, the alternating (magnetic) plasma drive electric arc jet (MPD), and the pulse plasma thruster (PPT). The MPD can produce a greater thrust and a higher specific impulse, but it is still in the laboratory stage. In recent years, there has been more rapid development in the pulse plasma thruster using solid teflon as the working mass. The working mass system is simple, and it is suitable for weightless and vacuum environments. It uses an energy storing capacitor's instantaneous discharge of strong electrical currents to form high temperature electric arc erosion and to ionize the working mass; the working mass is then accelerated by the electromagnetic force and heating force and exhausted to produce thrust. This type of thruster was installed in the synchronous satellite for maintaining its eastern and western positions in 1968. Its principles are illustrated in Figure 8. The performance of prototypes currently being developed is: unit impulse of 30.5 millinewtons/second, average thrust of 4.5 millinewtons, average specific impulse of 1,500 seconds, power consumption of 135 watts. It has already been proven that such a prototype has an efficiency of 30 percent; further research in the acceleration mechanism can improve its efficiency and performance. This type of thruster is suitable for various types of high precision and long life positional and orbital control of satellites.
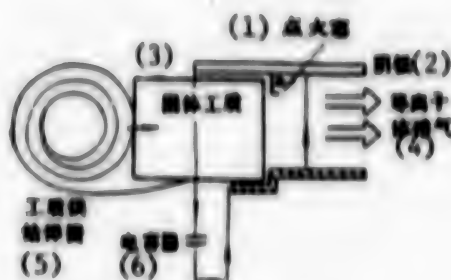
Figure 8. Illustration of the Principle of the Solid Pulse Plasma Thruster

Key:
(1) Spark plug
(2) Cathode
(3) Solid working mass

(4) Plasma exhaust
(5) Working mass supply spring
(6) Capacitor

The technology of plasma thrusters is related to some other important sciences and technologies, such as controllable thermonuclear reactions, high temperature plasma physics, high energy particle accelerators and their research achievements directly affect technical questions of the plasma accelerator. The study of plasma propulsion also has reference value to these sciences and technologies. This mutual influence between scientific field can be seen especially clearly in the plasma research of the Soviet Union.

4. Brief summary. Electrical propulsion technology has been developed for more than 20 years, and it has advanced from the stages of experiment in principles and laboratory research to the production of prototype units and space flight tests. The more advanced and more mature thrusters are the ion generators and the pulse plasma propulsion. Recent applications involve the positional and orbital control of various types of synchronous satellites. In the future, they may be used as the main propulsion units for orbital lift of satellites and interplanetary flight. Related scientific and technological research serves to stimulate other sciences and technologies, such as the research in propulsion which has helped plasma physics, dynamics of thin gases, vacuum discharge electrophysics and related testing technologies. It has also stimulated the development of some new materials, new technologies and new techniques.

In space technology, the problems related to plasma are broad in scope. A lot of work related to these problems has already been done abroad. Some of the problems have already been solved. Therefore they are no longer the "popular" fields of basic research abroad. But it seems that the work has not stopped; in particular, the many key problems are still being kept secret. Combining our nation's actual needs, besides solving the actual problems, research should be carried out to study the problems related to the science and the technology themselves and such research should be continued and become more profound. This will surely serve to improve the level of science and technology in this regard in our nation and stimulate the development of related sciences and technology greatly.

PHYSICAL SCIENCES

EXPERIMENTAL STUDY IN EXPLOSIVE WELDING REPORTED

[Article by Zhang Zhenkui [1728 2182 6652] and Wu Shaoyao [0702 4801 1031] of
the Luoyang Ship Materials Research Institute: "Experimental Study of Explo-
sive Welding Parameters"]

[Text] The study of explosive welding has an important significance in predict-
ing and controlling the welding process and obtaining good welding quality.

Objectively, a rational range of welding parameters always exists in the explo-
sive welding of any metal and alloy. To determine this range, a long search
has been carried out in theory and practice. Some theories and models (1-3)
have been developed, some criteria, bases for judgment and expressions of the
welding parameters (4,5) have been proposed. They provide some methods and
references which can be learned. But the mechanism of explosive welding still
needs more profound study; in trying to accurately and quantitatively predict the
necessary conditions for good welding, some difficulties are still encountered,
especially in a wide range of material combinations and different experimental
conditions. Therefore, some researchers believe the best collision condition
in explosive welding and determination of the rational parameters are questions
that need further study.

This article is a preliminary attempt to predict the rational parameters of ex-
plosive welding of flat plates in experiments on a few half-cylinders. At the
same time, experiments with flash-X-ray photography and with flat plate welding
were conducted. The results and analysis show this method is valid.

Analysis of the Method of Experiment

Figure 1 shows the explosive welding installation of the flat plate and the
half-cylinder and the welding parameters. When the dynamite is detonated at
one end, the flyer plate collides with the base plate (half-cylinder) obliquely
with a speed of V_p by the action of explosive products. As long as the para-
meters are appropriate, metallic plastic flow and reentry jets will be produced
in the area of collision, thus realizing a metallurgical bonding of two kinds
of metals and alloys. On the boundary surface of the bonded area, there
generally exists a unique and orderly wave pattern.

Under definite conditions, the welding quality is mainly determined by the welding parameters. To predict and control the welding parameters, we must first be able to quantitatively calculate or measure them and establish theoretical and analytic formulas or experimental expressions that reflect the relationships between them. We must obtain the relationship between the welding parameters and the organizational form of the bonded area. Then, we must obtain the boundary conditions of the welding parameters. Analysis shows the half-cylinder method can satisfy the above requirements.

Some research papers on the half-cylinder method have already been published. The main one among them is the use of the half-cylinder method to determine the bending angle of the flyer plate (6) proposed by J. F. Kowalick and D. R. Hay, starting out from predicting the conditions of formation of the wave patterns in the bonded area and utilizing dimensional analysis to obtain the expression (7) of the unit area amount of explosives c as a function of the thickness of the flyer plate δ, density ρ, volumetric speed of sound V_s and the collision angle β. At the same time, the flow characteristics (8,9) of the metal in the bonded area were also studied. Some others have also used the half-cylinder method to study the dimension of the waveform and its relationship with the welding parameters and the pattern of motion of the flyer plate (10-12).

The suitability of the half-cylinder method should be considered. The parameters of half-cylinder welding and the parameters of flat plate welding are comparable and they also differ. This kind of difference is mainly caused by the indefinite and unstable effects of V_{cp} brought about by the radius of curvature of the half-cylinder. When the radius of the curvature is sufficiently large or when the ratio between the dimension of the waveform in the bonded area and the radius of the curvature is sufficiently small, this indefinite and unstable effect can be neglected; at the same time, consideration must also be given to the stable explosion of the dynamite and the effects of the shape of the container of explosives. In this way, on a section of limited arc length, V_p can be regarded as a constant.
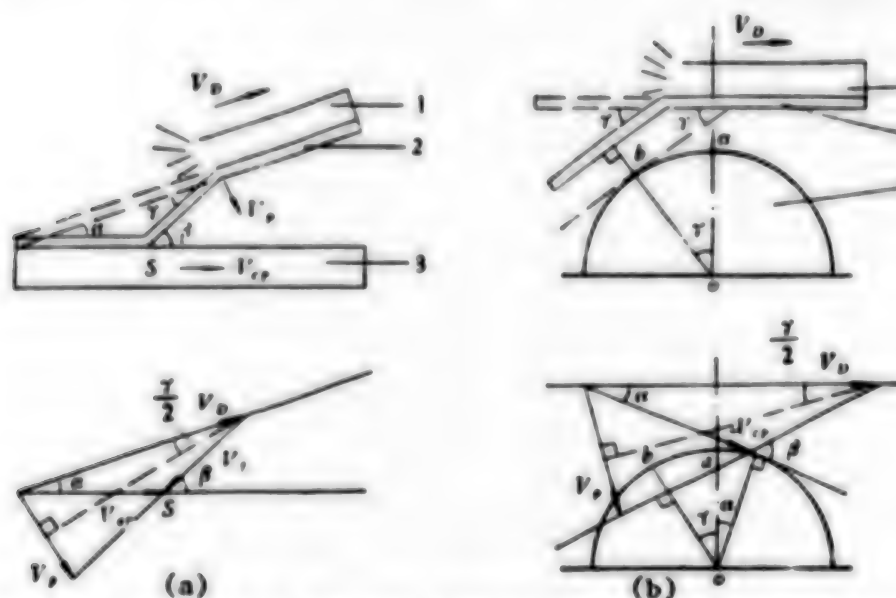

Figure 1.   Explosive Welding Installations and Welding Parameters

Key: 1. Explosives   2. Flyer plate   3. Base plate   4. Half cylinder

Comparison of Figures 1(a) and 1(b) shows that the vector graphs of velocity of the two types of welding installations have visible similarities. From the theorems of geometry we can obtain the following basic relationship of bonding parameters of general applicability:

$$V_p = 2V_p \sin \frac{\gamma}{2} \tag{1}$$

$$V_{cp} = V_D \sin\gamma/\sin\beta \tag{2}$$

$$V_f = V_p \cos (\beta - \frac{\gamma}{2})/\sin\beta \tag{3}$$

When the preset angle $\alpha = 0$, i.e., corresponding to the apex a of the half-cylinder

$$V_{cp} = V_D = V_f; \gamma = \beta$$

In equation (3), the V_f is the velocity of the flyer plate relative to the point s of collision. We should explain that equation (1) was obtained under the pre-requisite that the direction of the vector V_p is perpendicular to the bisecting line of bending angle γ. It has been proven by X-ray tracing photographic experiments (11) that when the preset angle α is zero, V_{cp} equals V_D, and this has also been proven by high speed photographic experiments (13). Therefore, the geometric model of the bonding parameters and the expression of their basic relationship are generally correct. Figure 2 is an X-ray photographic image of the copper flyer plate and the steel half-cylinder obtained in this experiment. It shows that before the flyer plate collides with the surface of the half-cylinder, its state of motion and the value of γ have already been determined; in other words, the value of γ is determined by the parameters of the explosives-flyer plate system. Therefore, the γ determined by the half-cylinder method and the bending angle of bonding with the flat plate are equal in value.

Figure 3 shows the waveform on the upper side of the half-cylinder perpendicular to the collision point b. When the distance from point b increases, and when V_{cp} lessens, the dimensions of the waveform at the bonding area increase and the degree of metallic plastic flow reduces. At the same time, the dimensions of the waveform also increase as the thickness of the flyer plate and the angle of collision increase. This type of regular variation is consistent with the actually measured data in flat plate welding. Analysis by fluid dynamics shows that the emergence of the wave and the size of V_{cp}, the density of the metal and the viscosity coefficient are related. The experiment revealed that in combining the same material, the V_{cp} value when waveforms emerge in the bonding area generally does not change; therefore, we can regard the critical collision point velocity V_c as the critical parameter separating the presence or absence of waveforms in the bonding area.

The image of the reentry jet can be clearly seen in Figure 2. It shows that the welding of the half-cylinder and the welding of the flat plate are the same; they have the same weldable conditions.
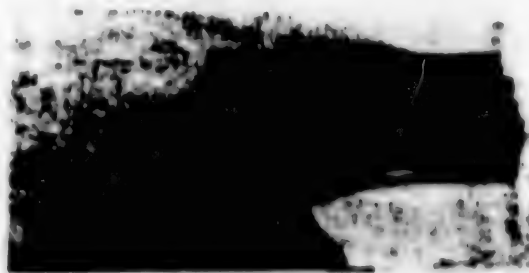
Figure 2. X-ray Photograph of the Motion of the Flyer Plate

Figure 3. Waveforms on the Upper Side of the Cylinder Perpendicular to the Collision Point

Explosive Bonding Experiments and Results

The flyer plate material for the experiment was BFe 30-1-1, the limiting strength was 54 kilograms/cm^2, and the dimensions were 100 x 250-100 x 300 millimeters. The base plate was a quenched and tempered steel with a limiting strength of 62-82 kilograms/cm^2. The diameter of the half-cylinder was 100 millimeters and the thickness was 50 millimeters. The experiment used a low explosive speed 2# ammonite explosive; its explosive velocity V_D and the corresponding thickness of the container of explosives satisfied the following relationship:

$$V_D = D_\kappa \left(1 - 0.48 \frac{H_s}{H} \right) \tag{4}$$

where D_k = 3,250 meters/second, the maximum explosion velocity of the explosive, H_0 = 1.4 centimeters, the critical thickness for explosion of the explosive.

Three groups of half-cylinder experiments were conducted. The first group's experimental parameters and results are shown in Table 1. We welded plates of different thickness and used amount of explosives and measured the bending angle and from nonlinear regressive analysis of the measured data, we obtained the experimental relationship for γ,

$$\frac{1}{\gamma} = a + \frac{b}{R} \tag{5}$$

23

Table 1. Parameters and Results of the Half Cylinder Experiment

a (mm)	Experimental parameters				V_c(m/s)	
	r(g/cm³)	A(mm)	V_D(m/s)	R	计算值	实验值
1.80	1.2	2.0	2020	0.75	338.7	382.3
	1.2	2.0	3580	1.38	577.9	732.5
	1.2	2.0	3870	2.00	709.5	1015.3
4.0	1.5	3.0	2250	0.42	294.8	271.9
	2.5	3.0	2670	0.70	459.2	479.6
	1.5	3.0	2930	0.98	580.1	669.1
7.0	2.0	5.0	2540	0.32	233.2	243.8
	4.0	5.0	3040	0.64	465.1	518.7
	6.0	5.0	3210	0.96	561.5	724.3

where γ = bending angle (degree)

$$R = \frac{\text{Amount of explosive of unit area}}{\text{Mass of flyer plate of unit area}} \quad \text{(pure member)}$$

a, b are constants related to the material combination and property of the explosives, a = 0.0473; b = 0.0426.
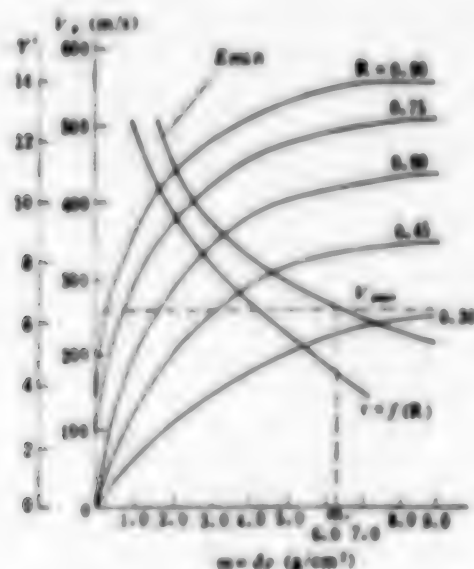

Figure 4. Curves of the Welding Parameters Obtained in the Half-Cylinder Experiment

Figure 4 shows the correlation curve of the bonding parameters drawn from the experimental results of the half-cylinder. It shows that when the amount of explosives is the same, γ reduces as the thickness of the flyer plate increases.

When the mass ratio R is the same, the value of γ is also the same. For different values of R, the bending angles can be calculated from equation (5) or looked up in Figure 2. The $\gamma = f(R)$ in Figure 4 is the form of the curve of equation (5).

After we obtain γ and V_D from equation (5) and equation (4), we substitute them into equation (1) and obtain the collision velocity V_p of the flyer plate. Figure 4 gives the V_p curve for different flyer plate thicknesses and different mass ratios. For comparison, Table 1 lists the flyer plate velocity calculated by the Deribas equation (14). The equation has the form

$$V_p = 1.2 V_D \left[\frac{\left(1 + \frac{32}{27} R\right)^{\frac{1}{2}} - 1}{\left(1 + \frac{32}{27} R\right)^{\frac{1}{2}} + 1} \right] \tag{6}$$

The second group of experiments concerned an X-ray photographic experiment during the course of explosive welding. It was conducted inside the explosion tunnel at the Mechanics Institute of the Chinese Academy of Sciences. The pulse voltage of the X-ray generator was 1,000 KV. Figure 5 gives the comparative curves of $V_p/V_D - R$ obtained by three methods: the half-cylinder experiment, the Deribas equation and X-ray photography. The results show that when R < 0.8, the three results basically coincide.

The third group concerned an experiment on the boundary conditions of the welding parameters. By experiment, we determined that the smallest flyer plate velocity producing a jet was 260 meters/second. The corresponding collision pressure calculated from the Hugoniot equation of the flyer plate and the base plate was 42.5 kilobars.

It should be pointed out that the smallest flyer plate velocity producing a jet is related to the combination of specific materials. Wittman suggested the use of the following empirical formula (1) to estimate it

$$V_{p_{min}} = |\sigma/\rho|^{\frac{1}{2}} \tag{7}$$

where σ is the limiting tensile strength (dyne/cm^2) of the material, and ρ is the density of the material (g/cm^3).

According to equation (7), the smallest flyer plate velocity obtained by the alternating method is 270 meters/second. The experimental and computed results coincide.
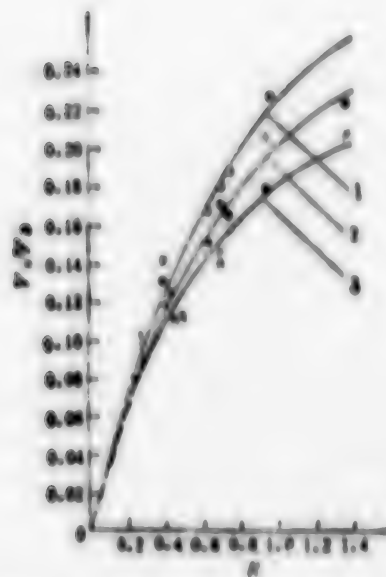
Figure 5. Comparative Curves of the Flyer Plate Velocities Obtained by the
Three Methods

1. Deribas equation   2. Half-cylinder   3. X-ray photography

Determinating and Proving the Rational Welding Parameters

The so-called rational welding parameters refer to the parameters that produce
a higher bonding strength and superior comprehensive properties. The rational
parameters are generally determined by the conditions of producing even and fine
waveforms by the collision reentry jet and the smallest amount of melting in the
bonded area and the interrupted distribution of melting. As described above,
the smallest velocity producing a jet in copper-steel explosive welding is 260
meters/second, the critical collision point velocity V_c producing waveforms in
the bonded area is about 1,360 meters/second, and the largest collision point
velocity for the waveforms to disappear approaches the volumetric speed of sound
of the flyer plate material. Measurements of the amount of melting in the bonded
area show that it increases as the kinetic energy of the flyer plate increases.
The maximum flyer plate kinetic energy allowed in copper-steel welding is about
77.25 kilograms·meter/cm^2.

At the same time, experience also shows that to effect welding, the kinetic
energy of the flyer plate must surpass a certain minimum value. It may be re-
lated to the smallest deformation in a unit volume required in the deformation
of materials. The smallest flyer plate kinetic energy of copper-steel welding
is 21.6 kilograms·meter/cm^2. It can be seen from Figure 4 that the point of
intersection of the smallest velocity curve and the smallest kinetic energy
curve corresponds to a definite flyer plate mass m_c. When $m < m_c$, the appro-
priate flyer plate velocity should be determined according to the smallest
flyer plate kinetic energy. When $m > m_c$, the flyer plate velocity should be

26

greater than $V_{p\ min}$. Therefore when determining the rational bonding parameters, the two factors described above should be considered together.

If bonding follows the principle of collision of equal energy, then the smallest flyer plate velocity and the smallest flyer plate kinetic energy can be united together to obtain the rational collision condition shown in Figure 6. In parallel installations and when the collision angle is small, equation (2) can be approximated by $V_p = V_{cp} \sin \beta$. When V_p is a constant, on the β-V_{cp} coordinates, it is a hyperbola. Similarly, we can obtain several sets of V_p curves of equal energy (two sets are shown in Figure y) and on each curve, the corresponding collision angle can be determined by the following equation

$$\gamma = \frac{57.428A + K_1}{\delta + K_2} \tag{8}$$

where δ = the thickness of the flyer plate (centimeter);

$$A = \frac{V_p}{D_k} \; ; \; K_1 = 1.24 \text{ (centimeters) constant;}$$

$$K_2 = 0.06 \text{ (centimeters) constant}$$

We can obtain the two curves, the smallest energy curve and the largest energy curve, by connecting the coordinates of the values of γ determined on the V_p curves of the same energy level, and from them we can obtain the appropriate collision conditions corresponding to the different thickness of the flyer plates. Rational initial parameters can be determined from the collision conditions thus obtained.

The most important initial welding parameter is the amount of explosives of unit area. It represents the energy needed in welding. After γ has been obtained, it can be determined from equation (5). The appropriate value of the preset angle α is generally zero. The distance h between the two plates should be selected within the range of one-half to one times the thickness. The experimental and computed results of the rational welding parameters of the 7 millimeter copper flyer plate are:

Smallest flyer plate kinetic energy: 21.6 kilograms.meter/cm^2;

Smallest flyer plate velocity: 260 meters/second;

Appropriate collision parameters: V_p = 312.8 meters/second;

   V_{cp} = 2667 meters/second;

   γ = 6.725°;

Initial bonding parameters: c = 2.62 grams/cm^2;

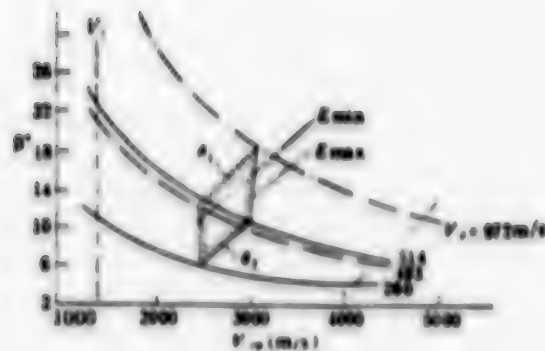 α = 0°; h = 0.5 centimeters

Figure 6. Suitable Collision Conditions (δ = 1.8-7.0 millimeters) Determined by the Principle of Equal Energy

To prove the rationality of the welding parameters determined above, we tested an orthogonal design of the welding parameters of a flat plate of 7 x ϕ500 millimeters. The amount of explosives of unit area (gram/cm^2) was 2.7; 3.2; 3.7; 4.2; the preset angle (degree) was 0 and 1; and the distance in between (centimeters) was 0.5 and 1.0. We conducted 16 experiments using different parameters by selecting the orthogonal table L16 (4 x 2^{12}) according to three factors and four levels. Samples were taken from the test plate after welding to find the percentage of overlapping area, and the shear strength of the metallic phase in the bonded area (height of waveform, melting area), the boundary surface tensile failure and such properties were examined. Analysis of variance of the data and the experimental results shows low level parameters have the best bonding strength and technological properties. The major performance parameters corresponding to these parameters are a shear strength of 39.1 kilograms/millimeter^2; boundary surface tensile failure of 60.0 kilograms/millimeter^2; average height of waveforms in the bonded area of 0.179 millimeters; and average melting area of 0.024 millimeter^2.

Several Conclusions

After analyzing the experiments and the results, we have reached the following preliminary conclusions.

1. When determining the rational welding parameters for use, two factors, the smallest flyer plate kinetic energy and the smallest flyer plate velocity, should be considered. The parameters should be determined according to the principle of collision of equal energy and the lower boundary conditions of the welding parameters.

2. When determining the lower limit of the welding parameters, it is necessary to conduct a few experiments.

3. The half-cylinder method can predict the welding parameters of the flat plate and realize the goal of controlling the welding quality. It has relatively wide adaptability.

REFERENCES

1. Crossland, B., Cave, J. A., Banerjee, S. K. and Wylie, H. K., The Explosive Welding of Some Difficult Combinations, The Sec. Int. Sym. of the Japan Welding Society, 25-27th, Osaka (1975.8).

2. Stivers, S. W. and Wittman, R. H., Computer Selection of the Optimum Explosive Loading and Weld Geometry, Proc. 5th Int. Conf. On H.E.R.F., Denver, Colorado, 24-26 (1975.6).

3. Deribas, A. A., Simonov, V. A. Pakcharenko, I. D., Investigation of Explosive Welding Parameters for Arbitrary Combinations. Proc. 5th Int. Conf. on H.E.R.F. 4.1 (1975).

4. Carpenter, S. H., Wittman, R. H., and Stivers, S. W., Determination of Optimum Explosion Welding Parameters, AD. Aoo 6259.

5. Loyer, A.,Hay, D. Robert, Gerala Gagnon, Weldability Windows, the Selection of Explosive Welding Process Parameters, Proc. 5th Int. Conf. on H.E.R.F. (1975).

6. Kowalick, J. F. and Hay, D. R., Metallographic Measurement of Explosive Welding Parameters, Explosive Welding, Proc. of the Sele. Conf. Hove (1968).

7. Howalick, J. F. and Hay, D. Robert, Explosive Bonding: Dimensional Analysis, Proc. 2d Int. Conf. of the C.H.E.F. (1969).

8. Kowalick, J. F. and Hay, D. R. A Flow Analog for Explosive Bonding, Proc. 3d Int. Conf. of the C.H.E.F. (1971).

9. Kowalick, James F. and Hay, D. R., The Nature and Formation of the Bond in the Explosive Bonding of Metals, AD. 713555.

10. Tadao Onzawa and Masahiro Fujita, Wave Formation in Explosive Welding of Metals, Proc. 5th Int. Conf. on H.E.R.F. (1975).

11. Yu Takizawa, Takeshi Izuma, Tadao Onzawa and Masahiro Fujita, An Experimental Study of the Acceleration Zone and the Terminal Velocity of Flyer Plate Driven by Explosive, Proc. 5th Int. Conf. on H.E.R.F. (1975).

12. Chladek, L. and Vacek, J., Choice of Kinematic Collision Condition for Explosive Welding, Proc. 5th Int. Conf. on H.E.R.F. (1975).

13. Frank J. Seiler Research Laboratory Explosive Impulse Welding (Volume 1) AD. AO 47955 (1977).

14. Ezra, A. A., Principle and Practice of Explosive Metalworking, 1 (1973).

9296
CSO: 4008/370

LAUNCHING TECHNIQUES OF BALLISTIC TARGET STUDIED

[Article by Zheng Zhichu [6774 0037 0443], Wang Xiqi [3076 6932 3823], Wang Jiurui [3769 0046 3843], Han Zhong [7281 1813], Zhang Zhensong [1728 2182 2646] of the Mechanics Institute of the Chinese Academy of Sciences: "Some Launching Techniques of a Ballistic Target"[a])

[Text] The ballistic target is an important experimental means to launch the study of high velocity collision and the phenomena of aerodynamics and aerodynamic physics. Because it has its special advantages over the wind tunnel and the shock tube and such equipment, at the end of the 1950's and the beginning of the 1960's, when it first showed its superiority in the realm of hypersonic speed, it caught people's attention. The equipment consists of three main parts: the model launcher, the target field and measuring and display instruments. The launcher is the key to the equipment. A frequently used launcher is the second class light gas gun; its structure is illustrated in Figure 1.
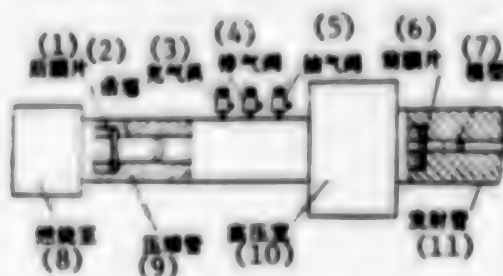
Figure 1. Simplified Diagram of the 1# Ballistic Target Model Launcher

Key:
(1) Rear diaphragm
(2) Piston
(3) Filling gas valve
(4) Exhaust valve
(5) Gas extraction valve
(6) Fore diaphragm
(7) Model
(8) Combustion chamber
(9) Compression tube
(10) High pressure chamber
(11) Delivery tube

For over 10 years, a lot of work has been done abroad in the study of the high velocity launcher (1-3). The purpose is to launch a model that has a complete outer shape, a stable position and a launching velocity that is as high as possible. Yet, the technical indicators of these three goals are mutually limiting, so the difficulty in the launching technique is very great. Here, we will introduce mainly the effective measures used on the 1# ballistic target launcher. These measures enabled it to satisfy the above demands. It has produced good results in the experimental study of the transonic flow, the rod-shaped launched impact target, and manmade superhard synthetic materials.

I.   Performance Test

The performance test is based on the need of the experiment to assure that the equipment will operate smoothly and to achieve the expected exit velocity under a definite model quality and outer shape. Experiments have proven that the key to assure that the equipment will operate smoothly is to limit the maximum pressure P_{max} in the high pressure chamber according to the actual situation; the motion equation of the analytical model is:

$$m_s \frac{du}{dt} = P_s A_s$$ (1)

Let $\bar{P}_s = \int_0^l P_s dx / l$.   integrating equation (1) yields

$$u_s = \left(\frac{2 A_s l}{m_s} \bar{P}_s\right)^{1/2}$$ (2)

Here, m_s is the mass of the projectile; A_s is the sectional area of the delivery tube; l is the length of the delivery tube; u_s is the exit velocity; P_s is the instantaneous pressure at the bottom; and $\bar{P}_s$ is the average pressure at the bottom. It can be seen from equation (2) that: the exit velocity u_s of the model is directly proportional to $\bar{P}_s^{1/2}$; to increase u_s, $\bar{P}_s$ must be greatly increased, and the corresponding P_{max} must also be greatly increased. For example, when comparing the two exit velocities of 7 kilometers/second and 5 kilometers/second, if m_s is the same, the corresponding u_s = 7 kilometers/second, $P_{max} \approx 11,000$ atmospheric pressure, while u_s = 5 kilometers/second, P_{max} = 6,000 atmospheric pressure. We should say that the present structure still cannot effectively seal gases with instantaneous pressure surpassing 7,000 atmospheric pressure. To avoid leakage of gas which will damage connected equipment and affect normal operation, P_{max} must be smaller than 7,000 atmospheric pressure. Of course, the corresponding u_s must also be smaller than 5 kilometers/second. A lot of experiments have proven that using this P_{max} as the upper limit to determine the initial filled air pressure and the amount of explosives as the filling conditions will enable the equipment to operate well.

To achieve the expected exit velocity, a simple method of calculation to reflect the operating nature of the light gas gun must be established. The light gas gun converts the energy produced by the combustion of explosives into kinetic energy of the model and the driving gases. The entire process should include energy loss due to friction, heat conduction, gas leaks and energy loss due to

the collision of the piston against the conical tube. Ordinary theoretical calculations have ignored these factors because of the difficulty of (mathematical) treatment. Energy conversion factors should be introduced to appropriately estimate these losses, and experiments can be conducted to measure the exit velocity to determine the energy conversion factors and the major filling conditions such as the initial filling air pressure, the thickness of the diaphragm of the delivery tube, the relationship between the working mass and the mass of the piston, and thus select filling conditions that can satisfy the structural strength, that can assure the demands of launching and have a relatively high energy conversion rate. Experiments have proven that the predicted exit velocity has a very good degree of accuracy.

II. Cavitation

To make the model complete and the position stable, the initial overload of the model must first be reduced. Cavitation is an effective method. It places the model at a definite distance from the diaphragm of the delivery tube; after the diaphragm breaks, the high pressure drive gas expands and then it is conducted to the bottom of the model. The initial overload is lower than where the model is placed near the diaphragm. At the same time, because the model begins its motion after leaving the delivery tube for a definite distance, the compression wave produced by the compression of the piston cannot immediately supplement expansion, the pressure at the bottom of the model cannot rise steeply, and it thus assures that the model will start up slowly within a definite time; when the piston enters the conical tube and when the peak pressure value arrives, overloading continues again, and the possibility of the model being destroyed is much less. This method has produced visible effects when N_2 is used as the driving gas. The results have been even better especially when this method is used for weak models with lower strength and which are longer and thinner, such as a thin and long copper pin. The above method has become an important means to assure that the model will not be deformed and the position will be stable. At present, we can launch L/D $\approx$ 10 copper pin models. Figure 2(a) shows inflight photos of the copper pin. For comparison, Figure 2(b) shows photos of crooked positions and deformed models in flight.
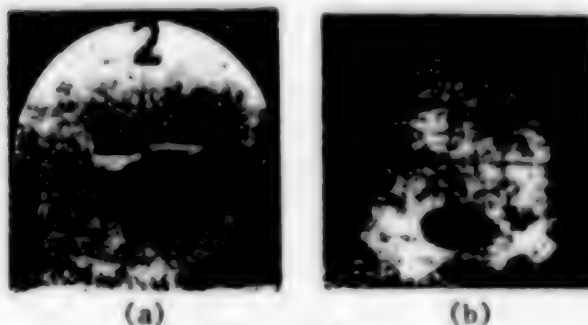

(a)   (b)

Figure 2

(a) Photograph of the launching of the thin and long copper pin by cavitation. (b) Photograph of deformed and crooked position of the copper pin.
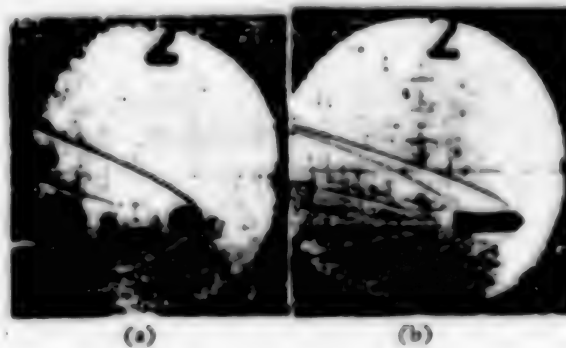

(a)   (b)

Figure 3. Photograph of the Model Which Has Successfully Detached Itself Aerodynamically From the Pad.

Cavitation also has other advantages:

1. It makes realization of aerodynamic detachment from the pad easy.

At the time of aerodynamic detachment from the pad, the ballistic support is valve-shaped and therefore, the structural strength is poorer; using cavitation and thin film techniques can reduce the initial overload, and the launching will be smooth. Figure 3 shows photos of the model launched after aerodynamic detachment from the pad.

2. It can determine the diaphragm breaking pressure from the historical pressure curve of the compression tube.

Measuring the diaphragm breaking pressure of the delibery tube is significant and difficult to accomplish. This is because the air pressure at the entrance of the delivery tube is very high; generally for reasons of strength and structure, the tube is not opened at will. Therefore, the method of pressure measurements by piezoelectric crystals cannot be used. Also, because the wall of the tube is thick, it is also difficult for the strain method to make accurate measurements. Yet, the use of cavitation to create the phenomenon in which the compressed wave cannot immediately supplement expansion enables us to determine the diaphragm breaking pressure from the sudden drop in the historical pressure curve of the compression tube and the pressure platform that persists for a certain time.

III. Thin Film Technique

Thin film technique involves the use of a relatively thin diaphragm. It is also used to reduce the initial overload of the model and to assure that the model stays intact and the position remains stable. At the beginning, because of the difficulty in processing valved diaphragms, the simple flat diaphragm was used. Diaphragms cut in this way hit against the model after acceleration and damage the ballistic support. The model also receives an extra blow and its flying position is affected. Figure 4 shows the details. This phenomenon becomes more serious as the launching velocity increases. For this, we have selected a copper diaphragm, which is not normally used (the thickness is generally 0.5 millimeters), and we have used chemical corrosion to etch the cruciform trough. This method has been tested many times and it has been discovered that valve forming is good and the technology is simple. Figure 5 shows a photo after the diaphragm has broken.

In addition, the width of the cruciform trough of the diaphragm was also studied. Generally it is much better if the width of the trough is less than 2 millimeters. Combined use of cavitation and thin film technique served importantly to solve the problems of keeping the model intact and the flying position. Figure 6 shows several typical in-flight photos.

Sometimes, to obtain special low velocity, very thin film is also used, which enables the light gas gun to operate under abnormally low efficiency. This method has served an important function in transonic launching. In addition,
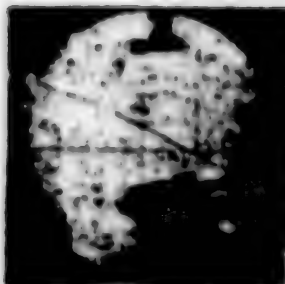
33

Figure 4.   Figure 5.   Figure 6.   Photographs of Typical
Shearing Dia-   Photograph of the   Flight
phragm Damages   Broken Thin Brass
the Ballistic   Diaphragm
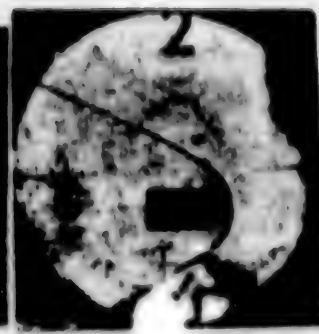Support

the use of thin film has also served well in solving the problem of sealing the
end surface of the delivery tube. The use of thin film can eliminate the use
of the rubber sealing washer between the end surface of the delivery tube and
the thin film. This method has been tested in launches using different working
masses of hydrogen, helium and nitrogen.

IV. Design of the Model

The design of the model greatly affects positional stability. Reference (4)
points out that when the model is started by the blasting load, a vibration of
a definite amplitude around the symmetric axis occurs, and as the model moves
inside the delivery tube, the amplitude of the vibration gradually lessens.
Generally speaking, the amplitude of vibration of a light model subsides slower
than that of a heavy model. A relatively poor launch occurs when the model
reaches the exit before the initial vibration has subsided and with the dis-
turbance at the exit, the vibration is strengthened; this causes a disorderly
flight position. Therefore, even if cavitation and the thin film technique are
used, if the design of the model is inappropriate, a stable position still can-
not be assured. In ordinary design there is concern only about the center of
gravity, which must be in front of the pressure center, but this is not the only
condition for positional stability in flight: consideration must be given to the
distribution of inertia of the model so that the inertia can be at a maximum in
pitch and in yaw. Figure 7 shows two in-flight photos of the conical model of
the same outer shape. The launch of the copper cone was successful, but the
position of the aluminum cone is not good; this is a very good explanation of
the effect produced by inertia.

Generally speaking, the projectile for launching consists of the model and the
ballistic support. When launching without detaching from the pad, the use of
polyethylene to glue each part together is an effective method to reduce the
vibration during launch and to assure the position. In addition, the outer
shape and the structural dimensions of the ballistic support also greatly affect
the production of disturbance. To prevent leakage of the driving gases, there
is a conical section with a very small taper at the tail end of the ballistic
support. The selection of the outer diameter and the taper of the straight
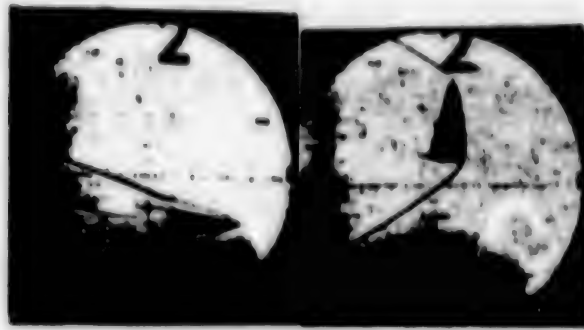
Figure 7. Effects of Different Inertia Upon the Flying Position

section of the ballistic support must be carefully considered. The details of the structural dimensions are shown in Figure 8. After many experiments, it has been proven that this is also a very important factor to assure positional stability of the model in flight.
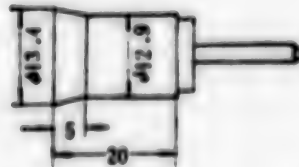
Figure 8. Structural Dimensions of the Ballistic Support

V. Improvement of the Structure of the Light Air Gun

Performance testing serves only to rationally select the parameters. How to assure that the launch will be according to the parameters selected still requires a lot of detailed considerations concerning structure. Here, we are talking about beneficial structural improvements to assure performance.

1. Air filling system. Hydrogen is a dangerous gas that explodes easily; foreign nations have given specific considerations to every part of the hydrogen filling system from the container to the tubes and the valves. For structural simplicity, the 1# target uses a filling system that can be generally used by various gases—hydrogen, helium and nitrogen. Operation of the system is safe and reliable.

2. Improvement of accessories of the compression tube. The compression tube of the 1# target launcher used to leak at the time of initial filling. This not only affected the launching parameters, but sometimes it also caused difficulty in dismantling. There are two reasons:

35

(1)   After repeated launches, the aperture of the part connecting the compression tube and the explosives chamber enlarges because of shearing of the diaphragm and washing by the explosives; the piston material (polyethylene) undergoes big changes because of the effect of temperature; and the diaphragm fixture loosens because of the deformation of the threads of the compression tube, thus causing a leak of the filling gas in the compression tube.

(2)   The exhaust valve where the compression tube is located lets out remnant gases from the explosives. But because the body of the valve and the valve rod are subjected to washing and corrosion by high temperature gases from the explosives, the seal is broken and becomes ineffective.

For these reasons, the diaphragm fixture and the hermetic structure of the exhaust valve shown in Figure 9 have been used. The former fixes the diaphragm tightly. The latter uses polytetrachloroethylene and a red copper hermetic cushion to increase the hermetic effect.

The model launcher of the 1# target generally speaking has a good launching repeatability as long as the filling conditions are strictly assured. These structural improvements are reliable assurances of the equipment's repeatability.
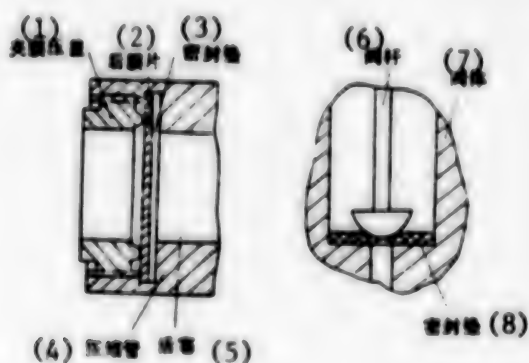
Figure 9.   Diaphragm Fixture and Exhaust Valve Sealing

Key:
(1)   Cover of fixture
(2)   Rear diaphragm
(3)   Hermetic pad
(4)   Compression tube

(5)   Piston
(6)   Valve rod
(7)   Body of valve
(8)   Hermetic pad

VI.   Conclusion

The 1# ballistic target has definitely progressed in launching techniques in recent years on the foundation of past work. It can launch various models of complete outer shape, of a stable position and of expected velocity according to the demands of simulation experiments within the subsonic, transonic and ultrasonic ranges. It also has the predicted repeatability. Under positionally stable conditions, it can control the landing point, and the velocity range is 0.16-5 kilometers/second. Along with the development in testing

techniques, it has established a foundation for the development of aerodynamic studies, studies of ultrahigh velocity collision, synthesis of various super-hard materials under dynamic and high pressure, and experimental research in the various basic theories under high temperature and high pressure conditions.

REFERENCES

1. Canning, T. N., Seiff, A. and James, C. S., Ballistic Range Technology, AGARD-AG-138-70 or AD-713915.

2. Crasby, J. K. and Gill, S. P., Feasibility Study of an Explosive Gun, NASA CR-709 (1976).

3. Flagg, R. F. and Mitchell, G. P., An Optimization of Study of the UTIAS Implosion-Driven Hypervelocity Launcher MKII, AD-708798.

4. Potter, J. Leith, Studies of Boundary-Layer Transition on Aeroballistic Range Models, AEDC-TR-73-194 or AD-778841.

9296
CSO: 4008/370

PHYSICAL SCIENCES

COMPUTATION OF TRANSONIC CIRCUMFLUENT FLOW FIELD

[Article by Li Yimin [2621 0001 3046]: "Computation of Three-Dimensional Steady Transonic Flow About Wings Using the Relaxation Method"*]

[Text]   Transonic flow is characterized by the simultaneous existence of sub-
sonic and supersonic flow accompanied by shock waves. From the mathematical
viewpoint, the characteristics of transonic flow must be described by the solu-
tion of "mixed" differential equations of the elliptic type in the subsonic
range and the hyperbolic type in the supersonic range. This type of equations
is nonlinear; their solutions contain an interrupted section--the shock wave.
The best method to treat the transonic flow imbedded with a shock wave is the
finite difference relaxation and iteration method. The first use of the relax-
ation method to solve transonic flow was by Emmons (1) but because he used the
Rankine-Hugoniot relationship to equip the shock wave, the method was not popu-
larly applied. Murman and Cole (2) proposed the method of finite difference
relaxation to automatically compute the shock wave, and thereby they opened up
a new path of research in computing the transonic circumfluent flow field.

This article is based on the characteristic of rapid attenuation of small dis-
turbance far from the object of circumfluent flow (including the tail vortex),
enabling the lattice to concentrate around the object of circumfluent flow with-
out affecting the precision of the difference operator and fully utilizing pre-
cise boundary conditions of the distant flow field. This article uses the trans-
formation of coordinates by the hyperbolic tangent function to transform infinite
physical space into a cube of (-1, +1) in length on each side and carries out
finite difference calculations inside the cube.

1.   Differential Equations of the Small Transonic Disturbance and Boundary
Conditions

The differential equation of the small transonic disturbance neglecting higher
order quantities is:

$$\left[1 - M_\infty^2 - (\gamma + 1)\frac{M_\infty^2}{a_\infty} \varphi_{x_1} \right] \varphi_{x_1 x_1} + \varphi_{x_2 x_2} + \varphi_{x_3 x_3} = 0 \tag{1}$$

_____

*This article was received on 17 June 1980

To facilitate computation, we perform the following transformation of coordinates: let

$$x = x_1/c, y = y_1/b, z = \delta^{1}M_\infty^{2/3}(\gamma + 1)^{1}z_1/c$$
$$\varphi = [M_\infty^{2/3}(\gamma + 1)^{1}/u_\infty c\delta^{2/3}]\varphi_1$$

and substitute these into the above equation; after rearrangement, we have

$$[K_1 - \varphi_x]\varphi_{xx} + K_2\varphi_{yy} + \varphi_{zz} = 0 \tag{2}$$

where

$$K_1 = \frac{1 - M_\infty^2}{[\delta M_\infty^2 (\gamma + 1)]^{2/3}}, \quad K_2 = \frac{c^2}{b^2[\delta M_\infty^2(\gamma+1)]^{2/3}}$$

which is a similarity parameter, wherein c is the half-chord length of the wing, b is the half-span length, and δ is the maximum relative thickness of the wing type.

On the material surface $z_{object\ surface} = f(x,y)$ the circumfluent condition

$$\left(\frac{\partial \varphi}{\partial z}\right)_{object\ surface} = \frac{\partial f(x,y)}{\partial x} - a/\delta,$$

is satisfied. a is the angle of attack. The tail edge of the wing satisfies the Kutta condition. Through the tail vortex φ_x, φ_z is continuous while φ is discontinuous; its transition value $\Gamma(y) = \oint d\varphi(x, y, \pm 0)$ is related to z; φ_{zz} is discontinuous except on the boundary of the distant flow field beyond $x \to \infty$, φ and its first and second order partial derivative of x, y, z all equal to zero. On the tail vortex $x \to \infty$ the value of φ must be solved according to $\Gamma(y)$ on the tail vortex. Using the following equation we can obtain the steady pressure coefficient from φ:

$$c_p = - \frac{2\delta^{2/3}}{M_\infty^{2/3}(\gamma + 1)^{1/3}}\varphi_{xx} \tag{3}$$

After integration, we obtain the amounts of the various dynamic forces.

2. Difference Scheme, Transformation of Coordinates and Relaxation and Iteration

Equation (2) is suitable for solution by finite difference iteration. When $\varphi_x < K_1$, the equation is elliptic (subsonic flow), so we use the central difference scheme; when $\varphi_x > K_1$, the equation is hyperbolic (supersonic flow), and differentiation of x uses the one-sided difference operator. Because the sonic speed line is a continuous transient line, no special rules apply. Using the

difference operator in place of differentiation brings about dissipation of high-order error terms; therefore, the shock wave of previously unknown intensity and position can form "naturally" during the course of solution. This method is called shock wave capture. This article has used the method of transformation of coordinates by the hyperbolic tangent function so that the lattice density near the object of circumfluent flow becomes larger while not reducing the precision of the solution: $\xi = th\bar{a}x$, $\eta = th\bar{b}y$, $\zeta = th\bar{\gamma}z$, changing the infinitely large space into a cube with sides of ± 1 in length. The change is one-to-one. When $\bar{a}, \bar{b}, \bar{\gamma}, \gg 1$ (not losing its generality), the object of circumfluent flow with its origin at the center of the computed space occupies 76 percent of the space of the cube. After transformation of the coordinates, equation (2) can be written as:

$$\bar{a}^2(1-\xi^2)[K_1 - \bar{a}(1-\xi^2)\varphi_\xi][(1-\xi^2)\varphi_{\xi\xi} - 2\xi\varphi_\xi]$$
$$+ K_2\bar{b}^2(1-\eta^2)[(1-\eta^2)\varphi_{\eta\eta} - 2\eta\varphi_\eta] + \bar{\gamma}^2(1-\zeta^2)[(1-\zeta^2)\varphi_{\zeta\zeta} - 2\zeta\varphi_\zeta] = 0 \qquad (4)$$

Calculation of the nonlinear differential equation (4) of variable coefficients is no more difficult than calculating equation (2). Here we have omitted solving the volumetric part of the approximate potential of the finitely distant border value, thus greatly conserving computer time. This part of the computation is equivalent to the time required to solve the entire flow field by iteration (3).

In the cube, an equidistant lattice is drawn which is equivalent to the nonequidistant lattice of large density near the object of circumfluent flow in physical space. A difference equation is established for each lattice point, and the method of linear relaxation and iteration is used (4). The relaxation line is parallel to the ζ axis. The potential of the point near the relaxation line is regarded as a known value to solve the set of difference equations. After calculating the potential $\psi^{(n)}$ of the nth iteration, we then calculate $\psi^{(n+1)}$ according to the iteration formula $\varphi^{(n+1)} = \omega\bar{\varphi}^{(n+1)} + (1-\omega)\varphi^{(n)}$ as the initial value to replace the potential $\psi^{(n)}$ on the relaxation line. In the equation, ω is the relaxation factor. In the subsonic range $1 \leqslant \omega < 2$ (overrelaxation); in the supersonic range $0 < \omega \leqslant 1$ (low relaxation). After preliminary computation of the value of ψ, we can carry out iterative scanning. First we scan from the upstream boundary toward the downstream boundary of the largest section of value η. When we have reached the line $\eta = 0$, we continue to scan each section in the direction of lessening values of η until the entire flow field has been scanned, thus completing one iteration. After each iteration, we use the value of this iteration to compute the distribution of the amount of circulation. The ψ obtained on the Trefftz plane is used as the boundary value for the next iteration. After several iterations, if every point of the flow field

satisfies $|\varphi^{(n)} - \varphi^{(n-1)}| < \epsilon$ (ϵ is the precision of control, generally, taken to be

(10^{-5}), then we can regard the solution as convergent. Many numerical experiments have determined the range of optimum values of ω: for the overrelaxation factor, $1.3 < \omega \leqslant 1.8$, for example, $\omega = 1.7$ can save one-third of the computer time compared to $\omega = 1$, and for the low relaxation factor, $0.5 \leqslant \omega \leqslant 0.8$.

During the course of computation, if the points on the entire relaxation line are all subsonic points, then the set of difference equations is linear. If supersonic points emerge on the relaxation line, then it is nonlinear. At this time, we should use closer values as the initial value for iteration to solve the equations. For example, we can use the result calculated by starting from a certain subcritical boundary M_∞ as the initial value for calculating a higher M_∞ (Mach number climbing method). Numerical experiments point out that as long as the value of ω is low at the beginning, we can also begin from $M_\infty = 0$ to calculate ϕ under a higher subcritical M_∞. In supercritical situation, such as an overly large climbing interval of the Mach number--for example, $\Delta M_\infty > 0.3$--a large interval may lead to divergence in iteration. At such time we must immediately make the climbing interval smaller and continue iteration. The computer time is directly proportional to the $(1 + r)$ equation $(0.4 < r < 0.5)$ of the lattice points, and it is also directly proportional to the logarithm of precision control ε.

Results of Computation

This article has calculated the pressure distribution over the 6-percent double circular arc wing, the rectangular wing that as aspect ratio of 4, the equal chord 30° sweptback wing, the 5-percent double circular arc wing, and the rectangular wing with an aspect ratio of 3. It can be seen from the diagrams that the results computed in this article and the experimental results (5,8) coincide very well and that they also coincide well with the computed results of references (6, 7). A better coincidence was realized between the experimental results and the subcritical results and the results with a zero angle of attack than between the supercritical results and the results with a nonzero angle of attack. This is because in the supersonic range, a difference scheme of a lower precision was used and because the variations in the flow near the leading edge and the shock wave region are more violent. The method of this article used nearly one-half less computer time compared to reference (6). For example, the results of Diagram 1 required 19 x 10 x 19 lattice dots using the method in this article, and the computer time on the 655 computer was 18 minutes, whereas reference (6) used 50 x 50 x 20 lattice dots, and the computer time on the IBM 360/67 was 30 minutes. This article also experimented with plane relaxation. Plane relaxation is faster than linear relaxation.

The difficulty encountered in the computation of the three-dimensional transonic circumfluent flow is how to handle complex outer boundary conditions. Linearization of the boundary conditions presents definite difficulties to solving for circumfluent flow near the blunt-nose leading edge and to improving calculations of the sweptback shock wave.
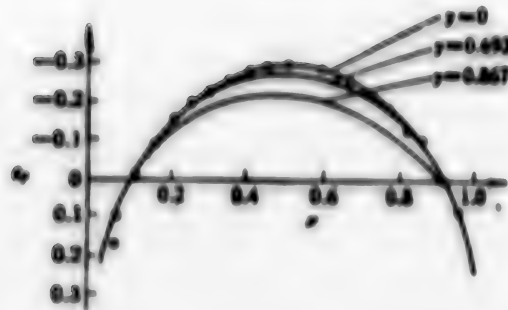
Figure 1. Distribution of Steady Pressure Over the 6-Percent Double Circular
Arc Wing Type and the Rectangular Wing With an Aspect Ratio of 4

o is the experimental value (5);   — is the computed value in this article;
y is the half wing span section.
M_∞ = 0.806, α = 0°, subcritical

Figure 2. Distribution of Steady
Pressure Over the 6-Percent Double
Circular Arc Wing Type and the
Rectangular Wing With an Aspect
Ratio of 4

o is computed value 4; y = 0;
Δ is the experimental value
  (two dimensional) (5);
— is the calculated value in
   this article.

M_∞ = 0.908, α = 0°, supercritical

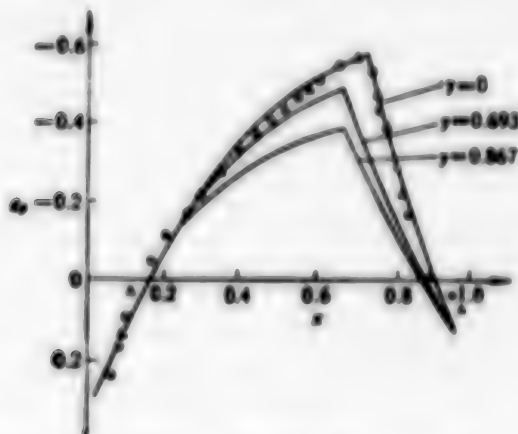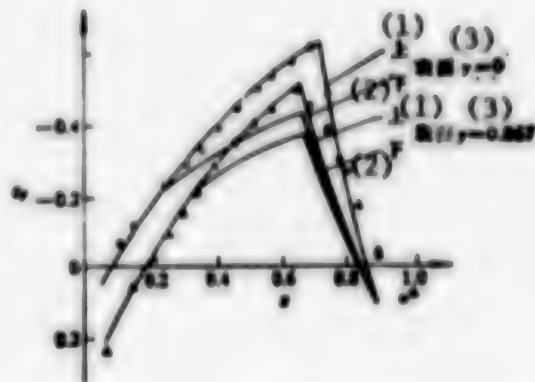Figure 3. Distribution of Steady
Pressure Over the 6-Percent Double
Circular Arc Wing Type and the
Rectangular Wing With an Aspect
Ratio of 4

o is experimental value of top surface(5);
Δ is experimental value of bottom surface;
— calculated value in this article.

M_∞ = 0.908, α = 1°, supercritical

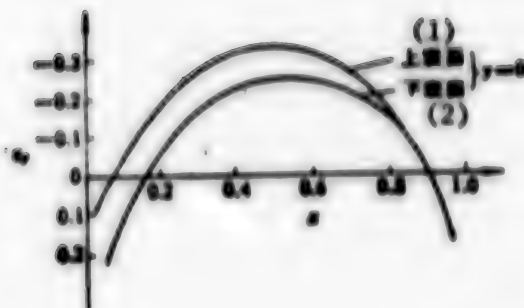1 top, 2 bottom, 3 surface y = 0,
surface y = 0.867

Figure 4. Pressure Distribution Over the Wing Root Section of the 6-Percent Double Circular Arc Wing Type, the 30° Sweptback Wing With an Aspect Ratio of 4

Key: (1) Top surface
     (2) Bottom surface

$M_\infty = 0.808$; $\alpha = 1°$;
$y = 0$ subcritical
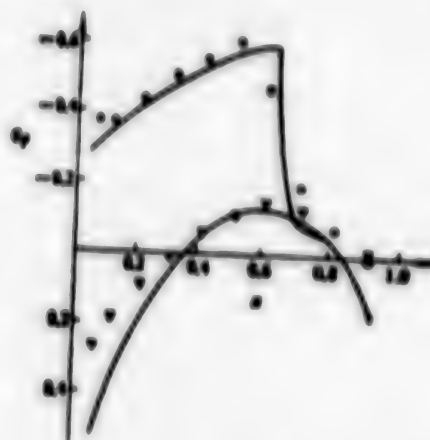
Figure 5. Steady Pressure Distribution Over the 5-Percent Double Circular Arc Wing Type, Rectangular Wing With an Aspect Ratio of 3

o experimental value of the top surface (8);
V is the experimental value of the bottom surface;
— is the calculated value in this article.

$M_\infty = 0.9$, $\alpha = 5°$,
$y = 0$, supercritical

REFERENCES

1. Emmons, E. W., The Numerical Solution of Compressible Fluid Flow Problems. NACA TN 932 (1944).

2. Murman, E. M. and Cole, J. D., Calculation of Plane Steady Transonic Flows. AIAA J, 9, 1 (1971)

3. Weatherill, W. H., Ehlers, F. E. and Sebatian, J. D., Computation of the Transonic Perturbation Flow Fields About Two- and Three-Dimensional Oscillating Wings. NASA CR-2599 (1975).

4. Newman, P. A. and Kunker, E. B., Computation of Transonic Flow About Finite Lifting Wings. AIAA J, 10, 7(1972).

5. Knechtel, E. C., Experimental Investigation at Transonic Speeds of Pressure Distribution Over Wedge and Circular Arc Airfoil Sections. NASA TN D-15 (1959).

6. Bailey, F. R., and Steger, J. L., Relaxation Techniques for Three Dimensional Transonic Flow About Wings. AIAA paper 72-189.

7. Lomax, H., Bailey, F. R. and Ballhaus, W. F., On the Numerical Simulation of Three-Dimensional Transonic Flow With Application to the C-141 Wing. NASA TN D-6933 (1973).

8. Lassing, H., Troutman, J. and Menees, G., Experimental Determination of the Pressure Distribution on a Rectangular Wing Oscillation in First Bending Made for Mach Numbers From 0.24 to 1.30. NASA TN D-344 (1960).

PROBLEM OF DETONATION WAVE DIFFRACTION EXAMINED

[Article by Guan Chuquan [4619 2806 8672] of the Mathematics Institute of the Chinese Academy of Sciences: "Approximate Analytical Solution of the Diffraction of a Plane Detonation Wave Around a Small Corner"*]

[Text] This article considers the problem of diffraction of a plane detonation wave. We have used an idea similar to that of Lighthill (1) to treat the problem of diffraction of a detonation wave near a small corner of a solid wall, we have obtained an approximate analytic solution, and we have analyzed the singularities of the solution.

I. Basic Motion Equations and Boundary Conditions

Let there be a plane detonation wave detonated at an infinite distance. In the medium of explosives, it is perpendicular to a plane rigid wall motion. This wall has a corner α (the corner turning downward is negative) at point Q. After the detonation wave moves to this point, it moves about this corner. On the extended line of the plane wall, the movement of the wave front of the plane wave is still maintained. On the lower side, there is a cylindrical wave with point Q as the detonation center. They all move at a normal detonation velocity D_J. These two waves are connected on the extended line of the plane wall. Because of the corner, the situation behind the waves is characterized by mutual interference. Now, we want to determine the flow in this disturbed region. Under such detonation and boundary conditions, the decisive parameters are the velocity D_J of the detonation wave, the pressure p_∞ in the stationary medium, the density ρ_∞, and the corner angle α. They cannot combine to form dimensions of basic length and time, and so therefore the motion is self-similar--i.e., all parameters of motion can only be functions of x/t and y/t.

If we take

$$X = x/t, \quad Y = y/t \tag{1}$$

*This article was received on 2 April 1979

as the coordinates system of motion, then in this coordinates system, the wave front becomes a standing wave. Because the plane and the cylindrical detonation waves are both Chapman-Jouguet detonation (3) waves, the motion on the wave front is even entropy irrotational motion. Therefore, the entire region behind the waves is an even entropy irrotational motion zone, and the detonation velocity D_J is a constant for a given medium of explosives. We also assume that the corner angle α is small; therefore the disturbance in the interference zone is also small. If we let

$$U = U_0 + U_1, \quad V = V_0 + V_1, \quad P = P_0 + P_1, \quad \rho = \rho_0 + \rho_1, \quad C = C_0 + C_1 \qquad (2)$$

where $q = (U,V)$, P, ρ, C represents the flow velocity, pressure, density and speed of sound, the subscript "0" represents the undisturbed quantity behind the plane wave and the subscript "1" represents the amount of disturbance. They are all small amounts. If we omit high-order quantities (and utilize $V_0 = 0$), the amount of disturbance should satisfy the equation

$$\frac{\partial q_1}{\partial t} + U_0 \frac{\partial q_1}{\partial x} = -\frac{1}{\rho_0} \nabla P_1, \quad \frac{\partial \rho_1}{\partial t} + U_0 \frac{\partial \rho_1}{\partial x} + \rho_0 \left(\frac{\partial U_1}{\partial x} + \frac{\partial V_1}{\partial y} \right) = 0,$$

$$P_1 = C_0^2 \rho_1 \qquad (3)$$

Because the motion is self-similar, utilizing transformation (1), and noticing that

$$t \frac{\partial}{\partial t} = -X \frac{\partial}{\partial X} - Y \frac{\partial}{\partial Y}, \quad t \frac{\partial}{\partial x} = \frac{\partial}{\partial X}, \quad t \frac{\partial}{\partial y} = \frac{\partial}{\partial Y} \qquad (4)$$

we can simplify equation (3) as:

$$(X - U_0) \frac{\partial U_1}{\partial X} + Y \frac{\partial U_1}{\partial Y} = \frac{1}{\rho_0} \frac{\partial P_1}{\partial X}, \quad (X - U_0) \frac{\partial V_1}{\partial X} + Y \frac{\partial V_1}{\partial Y} = \frac{1}{\rho_0} \frac{\partial P_1}{\partial Y},$$

$$(X - U_0) \frac{\partial P_1}{\partial X} + Y \frac{\partial P_1}{\partial Y} = \rho_0 C_0^2 \left(\frac{\partial U_1}{\partial X} + \frac{\partial V_1}{\partial Y} \right) \qquad (5)$$

Let

$$\frac{U}{D_J} = u_0 + u_1, \quad \frac{V_1}{D_J} = v_1, \quad \frac{P_1}{\rho_0 D_J^2} = p_1, \quad \frac{C_1}{D_J} = c_0, \quad \frac{X}{D_J} = \xi, \quad \frac{Y}{D_J} = \eta, \qquad (6)$$

Substituting equation (6) into equation (5) and deleting ρ_1 from the equation, we obtain

$$[c_0^2 - (u_0 - \xi)^2] u_{1\xi} + (u_0 - \xi)\eta(u_{1\eta} + v_{1\xi}) + (c_0^2 - \eta^2) v_{1\eta} = 0 \qquad (7)$$

Adding the irrotational conditions

$$u_{1\eta} = v_{1\xi} \qquad (8)$$

Figure 1

we have equations (7) and (8), which are the basic equations of the amounts of disturbance u_1, v_1. If we delete u_1 we will obtain a second-order equation of v

$$[c_0^2 - (\xi - u_0)^2]v_{\xi\xi} - 2(\xi - u_0)\eta v_{\xi\eta} + (c_0^2 - \eta^2)v_{\eta\eta} - 2(\xi - u_0)v_\xi$$
$$- 2\eta v_\eta = 0, \tag{9}$$

After transformation into polar coordinates

$$\xi - u_0 = r\cos\theta, \quad \eta = r\sin\theta, \quad (\xi - u_0)^2 + \eta^2 = r^2 \tag{10}$$

then equation (9) is translated to

$$\left(r^2 - \frac{r^4}{c_0^2}\right)v_{rr} + \left(r - \frac{2r^3}{c_0^2}\right)v_r + v_{\theta\theta} = 0 \tag{11}$$

The discriminant of this second-order equation is $\Delta = (r^2 - c_0^2)r^2/c_0^2$; i.e., when $r > c_0$ it is hyperbolic, when $r < c_0$ it is elliptic, and in the $r > c_0$ region, the two characteristic lines passing through each point (r_*, θ_*) are

$$\pm(\theta - \theta_*) = \text{arc}\cos(c_0/r) - \text{arc}\cos(c_0/r_*). \tag{12}$$

They are the family of straight lines enveloped by the circle $r = c_0$. This means that each characteristic line is tangent to the circle of disturbance $r = c_0$. Therefore, disturbance of any point outside the circle cannot affect the flow inside the circle. The circle of disturbance $r = c_0$ is an expanding circle in physical space and it expands with the speed of sound c_0 while the disturbance caused by the small corner is propagated at the speed of sound. Therefore, the disturbance caused by the corner can only exert its influence within the circle, and it does not affect the flow outside the circle. The disturbed region is the region encircled by the circle $r = c_0$ and the solid wall. The velocity component v_1 of the disturbance should satisfy the boundary conditions

$$v_1|_{r=c_0} = v_1|_{\theta=0} = 0, \quad v_1|_{\theta=T} = (u_0 + u_1)\sin\sigma \approx u_0\sigma. \tag{13}$$

47

Because the angle α was assumed to be very small, the original conditions satisfied on the slanted wall QT can be moved to the extended line QA of the plane wall, and the segment AT can be neglected. Thus, the problem is simplified to solving equation (11) on the semicircle $r \leqslant c_0$, $0 \leqslant \theta \leqslant \pi$. At this time the boundary conditions are

$$\eta\Big|_{\substack{r=c_0 \\ 0<\theta<\pi}} = \eta\Big|_{\substack{\theta=0 \\ 0<r<c_0}} = 0 \quad \eta\Big|_{\substack{\theta=\pi \\ 0<r<c_0}} = \eta\Big|_{\substack{\theta=\pi \\ 0<r<c_0}} = \alpha u_0 \tag{14}$$

II. Solving v_1

We introduce the complex number

$$\zeta = Re^{i\theta} = \lambda + i\mu, \quad R = \left[1 - \sqrt{1 - \left(\frac{r}{c_0}\right)^2}\right] \Big/ \left(\frac{r}{c_0}\right). \tag{15}$$

Thus, equation (11) is translated into a Laplace equation in polar coordinates. Then we perform a transform

$$\sigma = (\zeta + \zeta^{-1})/2 = \tau + i\nu \tag{16}$$

Thus, equation (11) becomes

$$v_{1\tau\tau} + v_{1\nu\nu} = 0 \tag{17}$$

The region to be solved under the transformation of equation (15) and equation (16) becomes the lower half of the σ plane. The corresponding relationships of the boundary are:

Circumference $r = c_0$, $0 < \theta \leqslant \pi$ → the (−1, 1) segment on the real number axis;

Radius oA → the (1, ∞) segment on the real number axis; oB → the (− ∞, −1) segment on the real number axis;

Center of the circle ($\xi = u_0$, $\eta = 0$) → infinity on the real number axis;

The point of the corner Q → the point Q' ($-\dfrac{c_0}{u_0}$, 0) on the real number axis.

The boundary conditions become

$$\eta\Big|_{\substack{-\frac{c_0}{u_0}<\tau<\infty}} = 0, \quad \eta\Big|_{\substack{-\infty<\tau<-\frac{c_0}{u_0}}} = \eta\Big|_{\substack{1<\tau<\infty}} = \alpha u_0 \tag{18}$$

The harmonic function satisfying condition (18) on the lower half plane is given by the Poisson formula. Expressing the v_1 obtained by the original variables, we have

$$\eta_1(\xi,\eta) = \omega_0 - \frac{\omega_0}{\pi}\left\{ \text{arc tg}\frac{\frac{c_0}{\omega_0}r^2 + c_0(\xi-\omega_0)}{\eta\sqrt{c_0^2 - r^2}} + \text{arc tg}\frac{r^2 - c_0(\xi-\omega_0)}{\eta\sqrt{c_0^2 - r^2}}\right\}. \tag{19}$$

From $p_{1\eta}/p_0 = (\xi-\omega_0)p_{1\xi} + \eta p_{1\eta},$ and $u_{1\eta} = p_{1\xi},$ and $p_1|_{\eta=\eta_0} = 0$, we can obtain

$$p_1 = \frac{\omega_0 p_0 c_0}{\pi}\left\{\frac{\sqrt{c_0^2 - r^2}}{c_0 + \omega_0 - \xi} + \frac{\omega_0}{2\sqrt{c_0^2 - \omega_0^2}}\right.$$
$$\times \ln\frac{c_0^2 + \omega_0(\xi - \omega_0) + \sqrt{c_0^2 - \omega_0^2}\sqrt{c_0^2 - r^2}}{c_0^2 + \omega_0(\xi - \omega_0) - \sqrt{c_0^2 - \omega_0^2}\sqrt{c_0^2 - r^2}}$$
$$u_1 = \frac{\omega_0 c_0}{\pi}\left\{\frac{\sqrt{c_0^2 - r^2}}{c_0 + \omega_0 - \xi} - \frac{\omega_0}{2\sqrt{c_0^2 - \omega_0^2}}\right.$$
$$\left. \times \ln\frac{c_0^2 + \omega_0(\xi - \omega_0) + \sqrt{c_0^2 - \omega_0^2}\sqrt{c_0^2 - r^2}}{c_0^2 + \omega_0(\xi - \omega_0) - \sqrt{c_0^2 - \omega_0^2}\sqrt{c_0^2 - r^2}}\right\}. \tag{20}$$

III. Discussion of the Solution

It can be seen from equations (19) and (20) that at the point of the corner $\xi = 0$, $\eta = 0$, the disturbance pressure p_1 and the velocity component u_1 all have logarithmic singularities. If the wall turns downward, then we have

$\lim_{\xi\to 0} p_1 (\xi, 0) = -\infty$. This overturns the assumption of a small disturbance. In fact, p_1 cannot assume such a negative value. The smallest negative value which p_1 can reach is $-p_0$. Here, the emergence of an infinite disturbance pressure is caused on the one hand by the treatment of the boundary conditions, and on the other hand, because in actual physical phenomena, the variation of flow near the corner is in fact more violent, and the irrotational condition near this point is no longer appropriate. But we can regard the singularity of the amount of disturbance as a mathematical description of this kind of violent variation. The experimental results on shock waves obtained by Fletcher(2) et al indicate that the pressure of the solid wall near the corner indeed undergoes drastic variation. It should also be pointed out that the effect of this type of singularity is only a localized problem--i.e., except for the area near the point of the corner, the effect is not large.

Besides the corner point, p_1 (and also u_1) also have singularities at point A. Point A is very close to the wave front, and it seems that there should be any disturbance ($p_1 = 0$); in actual phenomena, such a singular point should not exist. But because we moved the conditions on QT onto QA when we treated the boundary conditions, and because we neglected the AT segment, we have contracted the AT segment to point A. The property of this singular point is very similar to the property of the central simple wave at the central point.

It can be seen from the expression of p_1 and the isobar distribution that p_1 completely satisfies the conditions in the circle of disturbance and on the wall, and that while approaching point A along different paths it takes on different values.

Therefore, we say that the emergence of such a singular point is the result of mathematical treatment, on the one hand, and it also is a mathematical description of the physical properties near these points.

The multiple exponents γ of the equations of the products of detonation of ordinary explosives are all approximately 3. For simplicity, we used $\gamma = 3$ for calculation. Thus $p = A(s)\, \rho^3$, and at this time

$$u_0 = \frac{1}{\gamma + 1} = \frac{1}{4}, \quad c_0 = \frac{\gamma}{\gamma + 1} = \frac{3}{4}.$$

The distribution of p_1 on each of the section η is constant within the disturbance circle. The isobars in the disturbance circle are respectively shown in Figures 2 and 3 (where $\rho_0 = a u_0 c_0 \rho_0 / \pi$).
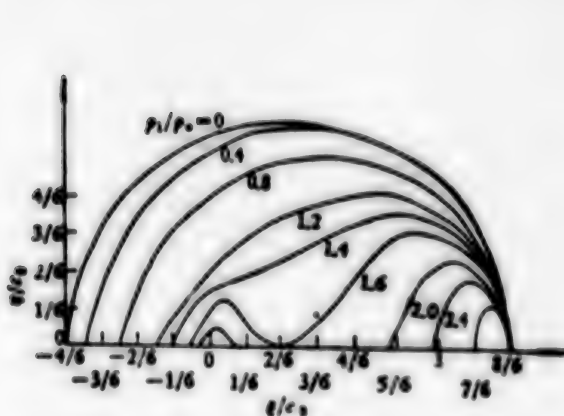

Figure 2. Isobars Inside the Disturbance Circle

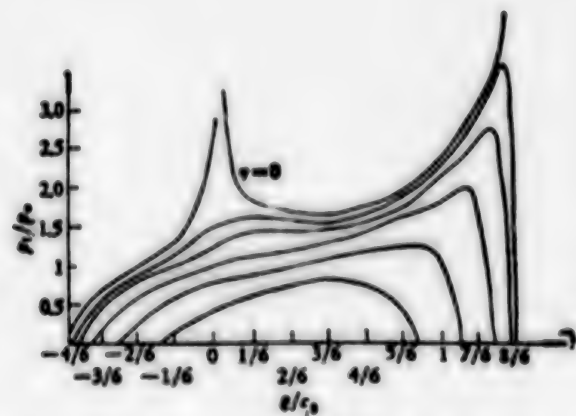Figure 3. Distribution of p_1 on Each Section Inside the Disturbance Circle

REFERENCES

1. Lighthill, M. J., The Diffraction of Blast. Proc. Roy. Soc., A 198(1949).

2. Fletcher, C. H., Weimer, D. K. and Bleakney, W., Pressure Behind a Shock Wave Diffraction Through Small Angle. Phys. Rev., 78, 5(1950), second series, pp 634-635.

3. Courant, R. and Friedrichs, K. O., Supersonic Flow and Shock Waves. (1948).

FINDINGS IN DRILLING METAL BY LASER DESCRIBED

[Article by Lu Renxiang [4151 0088 4382] of the Shanghai Optical Precision Instruments Institute of the Chinese Academy of Sciences: "Theoretical Calculations of Drilling Metal by Laser"*]

[Text] Abstract

This article establishes a "rectangular" phenomenological model showing the mutual reaction between a millisecond pulsed laser beam and metals. When the power density is greater than the damage threshold, the metal possesses a constant ablation rate. This article also establishes differential equations using the propagation of a Gaussian beam and discusses the relationship among the depth of the hole drilled, the shape of the hole, the position of the target, the focal length of the lens, the directionality of the laser and the energy of the laser.

I. The Phenomenon and the Model of Drilling Metal by Laser

Laser can drill holes without contact quickly in hard substances that are difficult to process by mechanical methods. It can form long thin holes without producing wear as drilling tools do. For this reason, it has been widely used in industrial production.

Laser processing has already accumulated a massive amount of practical experience (1-3). For example, with the same amount of energy of the laser and conditions of directionality, placing the focal point of the lens on the surface of the workpiece to be processed will not produce the maximum depth of drilling. The focal point must be at a definite depth inside the workpiece. Again for example, to drill through a thin workpiece so that the difference between the entry and the exit holes is less than a definite tolerance requires that the focal point be at a definite distance away from the surface of the workpiece. Conversely, if the focal point is set inside the workpiece, the hole drilled will have a shape with a large taper.

---

* This article was received on 21 July 1980.

We must ask: in drilling metals with a laser of a definite energy and direc-
tionality, what factors are related to the shape and depth of the hole drilled?
How can we obtain the maximum depth of the hole? This article will use the sin-
gle mode Gaussian beam as a model to explore these questions.

Laser drilling is a very complex process. It is related to many characteristic
constants of heat (specific heat, vaporization and latent heat of melting, heat
diffusion k, thermal conductivity K) and optics (surface reflection, light
absorption coefficient δ^{-1}) of the materials (6,10,16,17), and it is also related
to the distribution of the mode of the laser, the peak characteristics and the
method of focusing the lens.

For example, when we use an F_0 even and infinite heat flow beam to irradicate a
workpiece, the surface temperature T can be obtained by solving a one-dimensional
equation of thermal conduction (11,21)

$$T = \frac{aF_0}{K}\left(\frac{kt}{\pi}\right)^{\frac{1}{2}},\tag{1.1}$$

where K, k have been defined and given in the references quoted above, t is the
time of the heat flow pulse. When the heat flow is larger than a definite value,
the target will melt or evaporate. If the heat flow is the laser beam itself,
then when we use I_{th} to represent the threshold value light intensity; when the
surface temperature of the target approaches the boiling point, we have

$$I_{th}\sqrt{t} = const.\tag{1.2}$$

This means the shorter the laser pulse the greater the threshold light intensity
it needs.

But references (16,18) point out that the above relationship equation is valid
only within a definite pulse width, because when t is too small, heat diffusion
cannot carry the energy away in time before the laser pulse has passed.

The evaporation threshold I_{th} is divided into three time intervals (see
Figure 1):

$$I_{th} \propto \begin{cases} 1/t & t \ll \delta^2/k, \\ 1/\sqrt{t} & a^2/k \gg t \gg \delta^2/k, \\ \text{not related to t} & t \gg a^2/k, \end{cases}\tag{1.3}$$

δ, k have already been introduced above (δ is the inverse of the light absorp-
tion coefficient, $\sim 5 \times 10^{-4}$ centimeters; k for metallic aluminum is 0.91
centimeters^2/second), a^2 is the size of the focal spot of the laser. In our
typical situation it is 10^{-3} centimeters^2; therefore we can estimate the upper
and the lower limits of the second interval as 10^{-3} seconds $> t > 10^{-7}$ seconds.
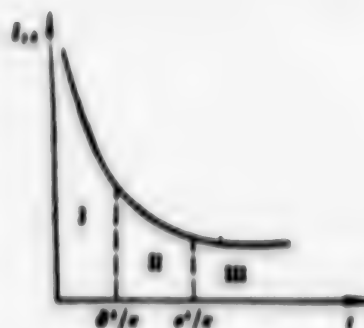
Figure 1

The energy laser we used to drill the holes acts within this time interval, i.e., equation (1.2) can be used. Figure 1 and equation (1.3) also show that using a large power millimicrosecond laser to drill holes is unfavorable because of a drastic increase in I_{th}.

In foreign nations, high speed cameras (6,7) and X-rays have been used to probe the holes (8) and study the deepening process of the laser. When $I > I_{th}$ a strong evaporation from the surface of the target occurs, and the ablation rate caused by splashing begins to increase. This kind of splashing occurs only during the time when the laser is at a peak, and the damage is intermittent. Synchronism between the laser and the glow of the products of evaporation has been discussed in many references (6,9).

When the light intensity continues to increase, the high temperature steam from the formation of the small hole during the early period further absorbs laser energy, and a high temperature and high pressure region is formed inside the hole, spewing liquid metal that has not reached the boiling point away from the target hole; therefore the burning heat is smaller than the heat of sublimation. When the light intensity is larger than a definite value I_c (I_c is defined in the following), the ablation rate basically remains unchanged. At this time, as the depth of the hole increases, the inner aperture gradually shrinks and causes the stream of already formed materials being spewed out to gradually become thinner. After the laser has been shut off, large quantities of metallic liquid still continue to spew out and this lasts for more than several dozen milliseconds. Later, several meters away from the sample, many metallic spherules or irregular metallic pieces formed by cold condensation can be gathered.

In reference (15), a ruby laser of 10^{-3} seconds and 7 joules was focused to a power density of $I \sim 10^7$ watts/centimeter^2; it was used to drill holes in many metals of the Periodic Table and a periodic relationship curve was obtained. The results showed clearly that generally speaking, drilling holes in metals with higher melting points is more difficult, and the lower the melting point of the metal the deeper the hole.

Of the many exploratory experiments related to the use of the laser to drill holes, the most interesting to us is the relationship diagram between the ablation rate (in this article, it is represented by γ^{-1}, its inverse is the

53

burning heat) of the material and the power of the laser I illustrated in references (9,22). Here, Figure 2 is Figure 8 in reference (9). Figure 2 uses the experimental data of the metals Cu, Al, Fe and Mg. It shows that when the light intensity is larger than a definite value, the ablation rate is basically a constant. The experimental conditions producing these curves utilize the neodymium glass laser with an oscillation time of 1 millisecond.

Obviously, such an experimental distribution curve makes it easy for us to use a rectangle to approximate it. Figure 2 shows a rectangular approximation of metallic aluminum in dotted lines.
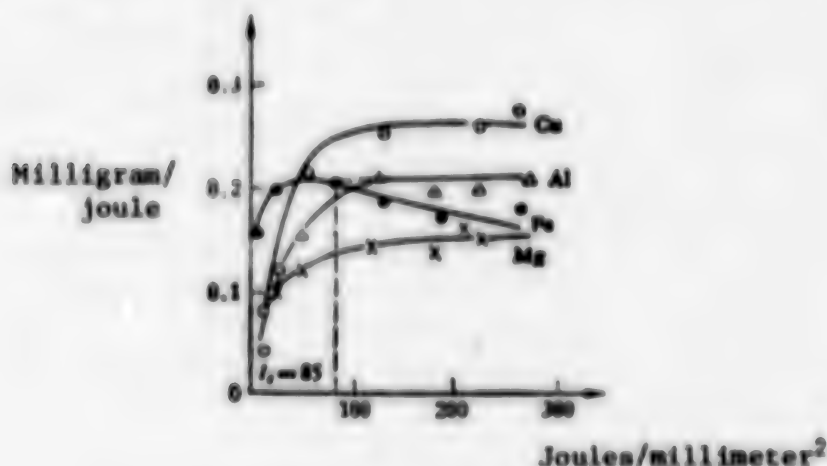

Figure 2

Therefore, we can carry out such a treatment: We can phenomenologically categorize the effects of the series of metallic parameters described above into two characteristic constants—the burning heat γ and the damage threshold I_c (note that I_c is different from the evaporation threshold I_{th} described above: $I_c > I_{th}$). They have the following relationship:

When $I < I_c$, $1/\gamma = 0$;

When $I \geq I_c$, $1/\gamma = \text{const}$.

For example, for metallic aluminum, we take $I_c = 85$ joules/$mm^2 \cdot ms$, $\gamma = (5.3$ joules/mg) x (2.7 mg/mm^3) = 14.3 joules/mm^3. Here, 2.7 mg/mm^3 is the density of aluminum. The value of γ calculated by reference (9) is close to our experimentally measured value of 12.5 joules/mm^3. We note that the burning heat of the laser is smaller than the heat of sublimation of aluminum. This is related to the large quantity of liquid metal contained in the splashed and spewed substance mentioned above. Table 2 in reference (9) lists the burning heat and the heat of sublimation of a series of metals.

II. Propagation of the Gaussian Laser Beam and Establishment of the Differential Equations

We know that in the open confocal cavity of a round end cavity plate, the mode distribution of laser strictly speaking should be an elliptic function or so-called "hyperspherical function" (14); when the Fresnel number of the cavity is large, it approximates a Laguerre-Gauss distribution

$$I = \left(\frac{\omega_0}{\omega}\right)^2 \left(\sqrt{2}\frac{r}{\omega}\right)^{2\ell}\left[L_p^\ell\left(\frac{2r^2}{\omega^2}\right)\right]^2 \exp\left(\frac{-2r^2}{\omega^2}\right). \tag{2.1}$$

In the expression above, the polynomial related to the Laguerre polynomial is

$$L_p^\ell = \frac{e^r r^{-\ell}}{p!}\frac{d^p}{dr^p}\left(r^{-\ell+p}e^{-r}\right).$$

For the higher order mode whose p and ℓ are all nonzero, the propagation of its plane of equal intensity and the isophase plane is more complex, less obvious than the propagation of the TEM_{00q} mode.

In the following, we will review the propagation of the basic TEM_{00q} mode of the laser. If the distribution of the energy of the laser beam along with time is even (rectangular pulse), then the focused TEM_{00q} mode has a light intensity distribution (2,4,5,13) near the focal plane of the lens (as shown in Figure 3)

$$\tag{2.2}$$
$$I(r,z) = \frac{E_0}{\pi\omega^2 t}\exp\left(\frac{-2r^2}{\omega^2}\right),$$

where

$$\omega^2 = \omega_0^2\left[1 + \left(\frac{z}{z_0}\right)^2\right]. \tag{2.3}$$

In the equation, t and E_0 are respectively the time of oscillation and the total energy, γ is measured from the light axis, z is the distance measured from the focal plane, ω_0 is the radius of the focal spot, note, differentiate this from the radius ω_0 of the waist of the light beam designated by the same symbol in equation (2.1); in the following, ω_0 will uniformly represent the radius of the focal spot), ω is the radius of the light spot under a light intensity of $1/e^2$ (center) after the Gaussian beam has propagated over a distance z. $z_0 = \pi\omega_0^2/\lambda$ is defined as the focal depth when the radius of the light spot expands from the focal point to $\sqrt{2}\omega_0$, λ is the wavelength of the laser.

The percentage of energy of the beam when the radius varies from 0 to r_c is

$$\rho = \frac{E(r_c)}{E_0} = \frac{\int_0^{r_c} 2\pi I r\,dr}{E_0} = 1 - \exp(-2\,r_c^2/\omega^2). \tag{2.4}$$

The relationship between the radius of the focal spot and the focal length of the lens f is $2\omega_0 = f \times \theta$, where θ is the angle of divergence of the TEM_{ω} mode. If that mode fills the lens of a diameter d, then

$$\theta = \frac{4\lambda}{\pi d} \approx 1.22\frac{\lambda}{d},$$

i.e., the single mode directionality approximates a limiting angle of diffraction; at this time, we have

$$\frac{z_0}{\omega_0} = \frac{2f}{d} = 2F,$$ (2.5)

$$\omega_0 = \frac{2}{\pi}\lambda F,$$ (2.6)

$$z_0 = \frac{4}{\pi}\lambda F^2,$$ (2.7)

F is the numerical aperture of the lens.

In the following, we will establish the differential equations for laser drilling. If damage begins with $I(r,z) \geqslant I_c$, then from equation (2.2) we know that the corresponding aperture is

$$r_c = \frac{\omega_0}{\sqrt{2}}\left[1 + \left(\frac{z}{z_0}\right)^2\right]^{\frac{1}{2}}\ln^{\frac{1}{2}}\frac{E}{E_c\left[1 + \left(\frac{z}{z_0}\right)^2\right]},$$ (2.8)

where the damage energy of the parametric threshold value $E_c = I_c t\pi\omega_0^2/2$, has been introduced.

In the course of drilling, the evaporation of each layer of the metallic target will cause the energy of the laser inside the threshold aperture γ_0 to reduce,

$$P(r_c)dE = -\sigma\pi r_c^2 dz.$$ (2.9)

When we substitute $P(\gamma_c)$ and γ_c into the above using equation (2.4) and equation (2.8), and let

$$z/z_0 = x, \quad E/E_c = y,$$

then we obtain the dependent relationship between the relative energy and the relative depth

$$\frac{dy}{dx} = -a\frac{y(1 + x^2)}{y - (1 + x^2)}\ln\frac{y}{1 + x^2},$$ (2.10)

where $a = rz_0/I_c t$, and if we let $u = \ln(y/(1 + x^2))$, then equation (2.10) simplifies to

$$\frac{du}{dx} = -\frac{2x}{1 + x^2} - a\frac{u}{e^u - 1}.$$ (2.11)
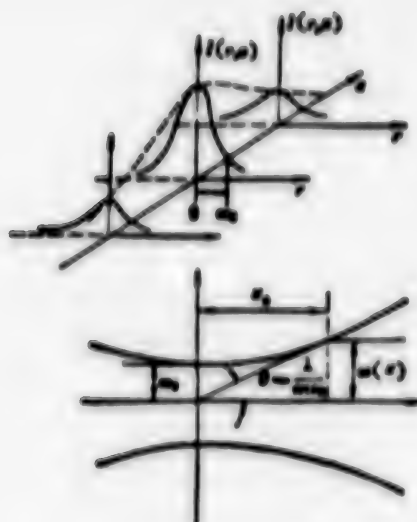
56

Figure 3

III. Solution of the Differential Equations and Equivalent Transformation of the Aperture

1. Numerical Calculation of the Differential Equations

Equation (2.10) cannot be solved by analytic methods under ordinary conditions. We have used the computer to perform numerical computations.

We set up a cylindrical coordinates system as shown in Figure 4; the surface of the target is the origin of the z axis, the depth of the hole is designated z; at a position away from the focal surface, a positive z_{00} indicates that the focal point is in front of the surface of the target, a negative z_{00} indicates the focal point is under the surface of the target. Other data for carrying out the computation are

$$I_c = 85 \text{ joules}/(\text{mm}^2 \cdot \text{sm}), \quad \gamma = 14.3 \text{ joules/mm}^3.$$

Using the neodynium glass laser, the aperture of the instrument and the lens is $d = 16$ millimeters, laser oscillation time is $t = 1$ millisecond, the laser output is single mode, $\theta_{11} = 0.075$ milliradian, and we take $f = 80.6$ millimeters, $E_0 = 57.5$ joules.

In actual computation, we used the Runge-Kutta (12) method, which has relatively high precision and is relatively stable for computer computation. We also used other numerical computational methods to check, and the solution was shown to be reliable.

In the above data conditions, using initial conditions of different target positions z_{00} to solve equation (2.10), and substituting each x, y value (i.e., z/z_0, E/E_c) on the integration curve into equation (2.8), we obtain the variation in aperture. Figure 5 gives the computed results of the variation of the depth of the hole and the shape of the hole with the positions of

the target. Note that in the computation, the condition indicating the bottom position of the hole is not an attenuation of the energy to zero ($y = 0$), but the condition $y/(1 + x^2) = 1$.
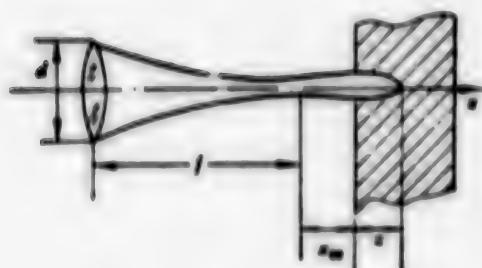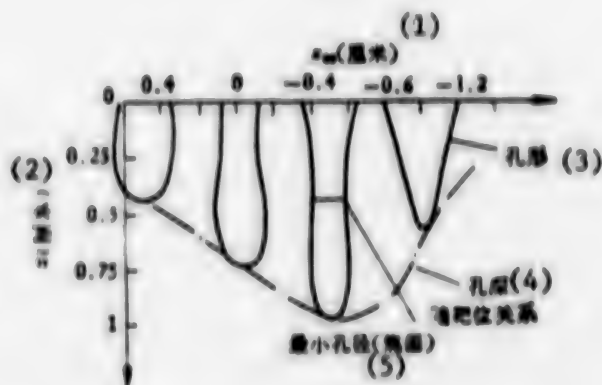

Figure 4

Figure 5.   Figure 5.

Key:
(1)   (centimeter)
(2)   (centimeter)
(3)   Shape of hole
(4)   Relationship between depth of hole and target position
(5)   Smallest aperture (focal plane)

In Figure 5, the horizontal coordinate represents the target position, the vertical coordinate represents the depth of the hole. Computed results show that to obtain the maximum depth of the hole z_m, the target position must satisfy the following conditions

$$z_{00} = -z_m/2 \tag{3.1}$$

This means that the focal plane must be at half the depth of the hole.

We know from the shape of the hole that when the focal plane is within a definite range in the hole, a kind of "vase shaped" (2) hole will emerge: the aperture will first become smaller until it reaches a smallest value and then it will enlarge. The patterns of variation of the shape of the hole and the depth of the hole with target positions similar to those shown in Figure 7 were proven by using a multiple mode oscillating laser of greater energy to drill holes.

By comparing the curve shown in Figure 5 with the corresponding curve shown in references (1-3) or with the written explanation on page 606 of reference (16) we will see that the computed results coincide with the actual situation. The different shapes of the hole corresponding to the target positions   be selected according to the different needs at the time of metal processi   y laser beams. For example, in industry, generally high precision holes with a small difference between the apertures of the entry and the exit through thin workpieces are required. It can be seen from Figure 5 that the focal plane
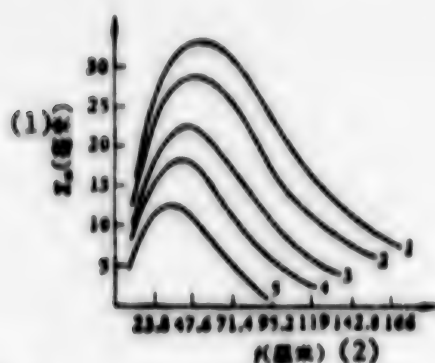
(1) Z(mm)

f(mm) (2)

Figure 6.
Key:
(1) millimeter
(2) f(centimeter)

Curve 1 is 200.9 joules; curve 2 is
143.5 joules; curve 3 is 86.1 joules;
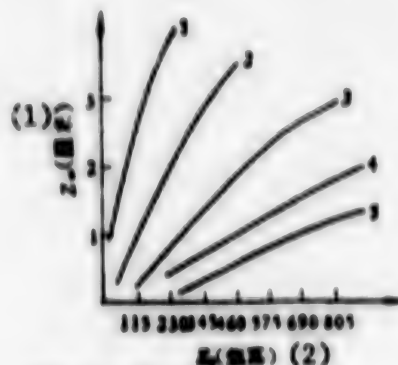curve 4 is 57.5 joules;
curve 5 is 28.7 joules

(1) Z(mm)

L(mm) (2)

Figure 7.
Key:
(1) (centimeter)
(2) (joule)

Curve 1 is f = 60.6 centimeters;
curve 2 is f = 121.2 centimeters;
curve 3 is f = 181.8 centimeters;
curve 4 is f = 242.4 centimeters;
curve 5 is f = 303.0 centimeters

should be out of focus and adjusted to a definite distance in front of the target. If the focal point is deep in the workpiece, an undesirable highly tapered hole will be produced.

If we hope to drill a hole of maximum depth under definite parameters of the laser and the lens, we can use equation (3.1) as a fixed rule. In actual work, the best target position can be found using the following experimental method. First, focus the focal point at the surface of the target and drill a hole of a definite depth, then move the focal point inward from the surface of the target to half the depth of the drilled hole and drill a deeper hole from that position. By continuing this, only three or four times are needed to quickly find the best target position. We also used this method to improve calculations and greatly reduced computational work.

In addition, we also used equation (3.1) as a guide to successfully drill the maximum depth of the hole. When using multiple layers of thin aluminum plates as the target material, the shape of the hole successively drilled in the target can be easily described. If we discover that the mouth of the "vase shaped hole" is not at half the depth of the hole but slightly closer to the opening, this means the focal point is not at the middle of the depth of the hole (equation 3.1 is not satisfied), and therefore this depth is not the maximum depth (because the focal point of infrared light is generally very difficult to measure). For the next drilling, the surface of the target should be moved slightly toward the lens so that the focal point will be at half the depth of the original hole, and thus a deeper hole can be drilled.

The relationship between the depth of the hole and the focal length and energy is discussed. To compare the level of drilling with different focal lengths of the lens, the variable factor of the position of the target must be set aside.

59

Everyone must use the maximum depth of the hole for comparison. We have carried out calculations for the typical instruments described above using different focal lengths f_0 and energy levels E_0. The results are shown in Figure 6 and Figure 7. Here, we assume that after the energy level has been increased, the directionality will not deteriorate and it will still be single mode oscillations.

Figure 6 shows the relationship between the depth of the hole using energy as the parameter and the focal length of drilling. It can be seen from the diagram that when the focal length of the lens used in drilling the hole lengthens, the depth of the hole lessens, and generally it lessens at a rate slightly faster than $1/f$. But when the focal length of the lens is too short, an abnormal situation occurs. This saturation of the depth of the hole using a lens of short focal length to drill holes has already been observed in our experiments. In high precision drilling of holes through materials used frequently in industry, a lens with a longer focal length should be used. At this time, because the focal depth is lengthened, the taper of the hole will be small when the energy is sufficient and the target position is appropriate.

Figure 7 uses the focal length as the parameter and shows the relationship of change between the depth of the hole and the energy. It can be seen that when the focal length of the lens is fixed, the depth of the hole basically increases in direct proportion to the increase in energy.

2. The Analytic Solution of the Depth of the Hole When the Focal Length Is Long

From equation (2.7) we know that the focal depth z_0 and f are directly proportional, z_0 increases faster than f, when the target is placed near the focal plane, the variation of the depth of the hole along with the target position is relatively slow, and

$$x = z/z_0 \ll 1.$$

At this time, the differential equation (2.11) can approximate an analytic solution. After deleting the first term on the right side of equation (2.11), the variables in the remaining differential equation can be separated, and the final solution for the depth of the hole is

$$z = \frac{l_d}{\tau}\left[\sum_{n=1}^{\infty}\frac{1}{n\cdot n!}\left(\ln\frac{E_0}{E_c}\right)^n\right] = \frac{l_d}{\tau}\left[\ln\frac{E_0}{E_c} + \frac{1}{2\cdot 2!}\left(\ln\frac{E_0}{E_c}\right)^2 + \frac{1}{3\cdot 3!}\left(\ln\frac{E_0}{E_c}\right)^3 + \cdots\right],$$

where

$$E_c = \frac{l_d\pi(f\cdot\theta/2)^2}{2}.$$

We note that the condition of convergence of equation (3.2) [sic] is $\ln(E_0/E_c) < 1$. If the previous instrument was used for drilling, but with $E_0 = 4.5$ joules, $f = 4$ meters, it is not difficult to obtain a solution when $E_c = 3$ joules,

$$z = 6 \text{ millimeters } [\ln 1.5 + \frac{1}{4}\ln^2 1.5 + \ldots] = 2.5 \text{ millimeters},$$

a 2.5-millimeter-thick aluminum target can be penetrated at a distance of 4 meters. Comparing this approximate solution and the numerical solution, we can see that they coincide very well, and at this time, "vase shaped holes" will not appear anymore. Figure 8 shows the shape of the hole drilled by laser with a lens of a focal length of $f = 31.5$ meters using a $\phi 10$ aperture single mode Gaussian beam of 600 joules. The variation in the shape of the hole when the target position z_{00} varies out of focus from 0 to 0.5 meters is minute.
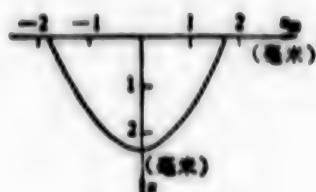

Figure 8

3. Equivalent Transformation of the Aperture

We know that when the laser beam is expanded n times by a variable aperture telescope, its angle of divergence θ will reduce by n positions. We know from the Lagrange theorem of the invariance of brightness (19) that after enlargement of the aperture, the brightness on the focal plane of a focal length of nf is the same as the brightness on the focal plane of a focal length of f. In this way, the hole drilled by a laser through a lens with a focal length of f and an aperture of d should be the same as that drilled by a laser through a lens with a focal length of nf and an aperture of nd, written in mathematical language,

$$Z_m(f, E_0, \theta, d) = Z_m\left(nf, E_0, \frac{\theta}{n}, nd\right), \tag{4.1}$$

where Z_m is the maximum depth of the hole.

Therefore, the shape of the hole drilled by a laser of 600 joules and a lens with a $\phi 10$-millimeter aperture and $f = 31.5$ meters shown in Figure 8 can be regarded as the shape of the hole drilled by a laser with a lens of $\phi 80$-millimeter aperture and $f = 252$ meters.

Here we must also point out that of the parameters a, z_0, E_c and E_0 appearing in the differential equation, a is related to the characteristics of the material, z_0 determines the depth of focus, and when the wavelength of the laser is fixed it is related to the focal length f of the lens. E_c is related to the focal length f and the damage threshold I_c when the aperture of the lens is fixed. E_0 is the initial value of the differential equation.

Obviously, for two types of metallic materials, if their material parameters satisfy $\gamma_1/I_{c1} = \gamma_2 I_{c2}$, making a the same, then their drilling pattern should also be the same. For a single type of specified metallic material, we know that when $Z_\omega = -Z_M/2$, there will be a maximum depth Z_n of the hole. It is only a function of f and E_0. We write it as $Z_M (E_0, f)$, and therefore we can use the computer to compute the table for this transcendental function within a broad range of E_0, f.

IV. Discussion and Conclusion

1. This article will affect the material parameters for laser drilling under rectangular approximation and will phenomenologically use the burning heat γ and damage threshold I_c to represent them. With this model, the shape of the hole will vary along with the target position when a Gaussian beam is used to drill a hole in metals, and the maximum depth of the hole can only be obtained when the focal plane is at half the depth of the drilled hole.

At the same time, as long as γ and I_c are determined by curves similar to those shown in Figure 2 for a certain metal through basic experiments, we can use the same computational program for calculating metallic aluminum to revise the values of γ and I_c, and thus conveniently obtain the depth table $Z_M (E_{02}, f_2)$ for holes in another metal.

It must also be pointed out that this kind of rectangular approximation has a definite arbitrariness in the selection of I_c. Strictly speaking, a rational I_c should be computed by calculating the extremely small mean square deviation of the curve prior to saturation shown in Figure 7. More strictly speaking, we should use a rational analytic formula to express the curve of the heat ablation rate from I_{th} to the saturation point and list the equations similar to equation (2.10) and solve them.

2. It has been discovered in experiments that when using certain methods to adjust the "peak" of the laser or when using a quasi-continuous laser (20) without peaks, the damage mechanism has new characteristics. But we have not discussed peak structures in this article, nor have we discussed the shape of the envelope of the energy pulse of the laser. We have limited our discussion to the free oscillating laser with general irregular peak structures.

3. The actual laser is a mixture of multiple mode oscillations. Here, there are working materials--lens type deformation of the glass rods, and there may also be localized regional self-focusing, and during the course of millisecond oscillations, the multiple mode combination and distribution pattern of the horizontal mode will also jump. Even for a high order horizontal mode of a specified confocal cavity, its Fresnel diffraction in spatial propagation will not be like the basic Gaussian mode, which has a visible rotating hyperbolic equal intensity plane expansion (satisfying Gaussian optics).

The propagation of an unstable cavity model is even more complex. We can see from Figure 8.43 in reference (19) that for an even amplitude spherical wave,

complex waveforms (see Figure 9) will occur in the distribution of the equal intensity plane near the focal point. Obviously, calculations will be even more complex when this type of light beam is used in drilling holes.
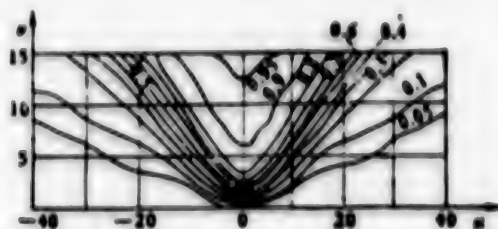

Figure 9. The Equal Intensity Plane
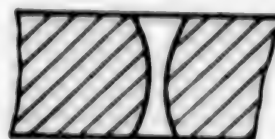of an Even Amplitude
Spherical Wave Near the
Focal Point

Figure 10

$u \infty z$, $v \infty r$, the numbers next to the curves are the proportion of light energy contained in the curved surface after the equal intensity line rotates about the u axis.

Even so, when we observe the scattering traces near the focal point of a multiple mode laser on the kilojoule level, we see that the equal intensity surface is still close to the rotating hyperbolic surface. This is consistent with the observation of the propagation of light beam near the focal point of the ruby laser mentioned in reference (17).

It is because of the similarity of propagation of the light beam that enabled the qualitative conclusion of the calculations for the single mode Gaussian beam discussed in this article to be binding over the present laser; for example, the conclusions concerning the qualitative relationships between the shape of the hole and the target position and the depth of the hole and the target position of the laser, the maximum depth of the hole requiring that the focal point be at half the depth of the hole have all been proven. The transcendental function table Z_M (E_0, f) of different materials allows us to predict and compare the different drilling capabilities.

4. Actual drilling is an even more complex procedure. Here, we have not calculated the reflection coefficient of the material, the variation of the coefficient of thermal conductivity and specific heat and such thermal physical properties as they vary with temperature (22), and we also have not considered the washing effect of the spewed substances upon the opening of the hole causing the shape of the opening of the hole to deviate slightly from the computed values.

In particular, we have not calculated the shielding effect (23) of the plasma plume of the spewed substances upon the laser beam. This effect will greatly reduce the mutual effect of the laser upon the target. In this situation, to obtain the shape of the hole and the depth of the hole consistent with those obtained in this article, more energy must be expended.

5. The qualitative conclusions concerning the variation of the shape of the hole with the target position mentioned previously are valid not only for metallic materials but it has been discovered in experiments that they are also valid for jewels in watches and diamonds. When a small tolerance between the entry and exit holes is required in drilling, the focus should be in front of the target.

In industry, sometimes wire drawing holes with a definite taper are required (see Figure 10); at this time, the focal point should be focused at a definite distance inside the target plate. After drilling once on the front of the material, the plate should be turned around and the same position on the back side drilled once to form the hole.

REFERENCES

1. Application of the Laser in Industry, Shanghai People's Press, 1972.

2. Huguchi Ryu-haka, Mitsubishi Electrical Engineering Technology Report, 45(1971), 1298.

3. V. M. Suminov, Machines and Tools, 6(1971), 37; Koboyashi Sho, Japan Machinery Society, 75(641)(1972), 953.

4. A. Maithand, M. H. Dunn, Laser Physics, 1969.

5. Larry Marshall, Laser Focus, 9(1971), 26.

6. J. P. Ready, 1964 Proc. Nat'l Electronics Conf., 22, 67.

7. A. M. Bonch-Bruevich, Y. A. Imas, Physics and Chemistry Processed Materials, 5(1967), 3.

8. I. G. Karasev et al, ZTF, 40 (1970), 1954.

9. S. I. Anasimov et al, ZTF, 36, (1966) 1273.

10. M. N. Libenson et al, ZTF, 38, (1968) 1116.

11. Jin Bixuan (6855 1732 6881), Nan Pojin (7181 3134 6651), Science of Electronics, 20(10)(1970), 74.

12. Compiled by the Mathematics Department of Fudan University, Computational Methods, 1961.

13. H. M. Haskal, A. N. Rosen, Appl. Opt., 10 (1971), 1354.

14. E. Wolf, Progress in Optics, 9, p 311.

15. A. I. Akimov, L. I. Mirkin, DAN SSSR, 183, (1968) 562.

16. V. A. Batanov et al, ZETF, 63, (1972) 586.

17. John F. Deady, Effects of High Power Laser Radiation.

18. A. M. Prokhorv, IEEE J., QE-9 (1972) 503.

19. M. Born, E. Wolf, Principles of Optics.

20. Dr Dieter Ross, Laser Light Amplifiers and Oscillators.

21. F. P. Gagliano et al, Proc. IEEE 57 (1969), 14.

22. Tan Hong (6151 3163), Zhu Zhonghou [2612 1350 0624), Pneumatic Laser Technology, Chapter 2, Section 1.

23. P. J. Klass, AW & ST, 99(2) (1973).

APPLIED SCIENCES

NEW TRENDS IN CHEMICAL WARFARE EXAMINED

[Article by Yang Shu (2799 2885): "New Trends in Chemical Warfare"]

[Text] A Type of Inexpensive Killing and Wounding Weapon

During World War 1, the use of chlorine gas, phosgene, and mustard gas killed over 90,000 people and wounded 1.2 million [figures as published]; many of the latter became permanently disabled. From that time on, people have called for a ban on the use of such cruel chemical weapons. In 1925, many nations signed the Geneva Protocol prohibiting the use of poison gas and other chemical weapons. But different nations have interpreted this protocol differently, and it has not served to prohibit the manufacture of chemical weapons. Starting in 1976, the United States and the Soviet Union held a series of bilateral technical negotiations and talks in Geneva, including chemical weapons disarmament and prohibition against the development, production, and stockpile of chemical weapons. But chemical weapons development, especially the development of new chemical weapons, is still being actively carried out. The reason is that chemical weapons have advantages with which other weapons cannot compare.

Chemical weapons are powerful and their killing and wounding range is large. A nuclear bomb equivalent to 20 million tons of TNT has a killing and wounding range of 190 to 260 square kilometers. But 5 tons of nerve gas can attain a killing and wounding range of 260 square kilometers. If this amount of poison is used to attack a city of 80,000 people, 40,000 people will be harmed and 30,000 will die.

Chemical toxicants are low in cost. The cost of producing a 1-ton nuclear bomb, equivalent to a 4-million-ton TNT bomb, is 1 million U.S. dollars. The cost of producing each ton of the nerve toxicant sarin is only 10,000 dollars! Some people have calculated the cost of mass killing and wounding per square kilometer. The cost of aerial bombing is between 10,000 and 100,000 dollars; the cost of conventional weapons is 2,000 dollars; the cost of nuclear weapons is 800 dollars; the cost of nerve gas is only 600 dollars.

Chemical weapons are not easily detected prior to use. They can be used suddenly to kill and wound masses of personnel and effect a sudden breakthrough of the enemy's defense line. Or they can be used together with conventional weapons and even nuclear weapons. This will strengthen the results of comprehensive utilization, and the enemy will not be able to defend himself effectively.

In addition, chemical weapons can inflict serious damage upon undefended military and civilian points. They have a killing and wounding effectiveness of 20 percent when used against soldiers who are unable to put on protective clothing and gas masks in time. But when soldiers wear antichemical equipment, their effectiveness in carrying out their mission drops by 30 percent. Some chemical toxicants have a long-lasting toxicity which can last several dozen days. Some chemical toxicants are not easily disinfected. Some do not have antidotes. Some will cause poisoning even if antichemical clothing is worn against them....The above advantages of chemical warfare toxicants far outnumber their shortcomings (such as weather limitations and geographical conditions). This is the direct cause for their rapid development.

New Types of Nerve Toxicants

According to foreign published reports, at present the officially deployed chemical toxicants of the United States and the Soviet Union can be classified into six main categories: organic phosphorous nerve toxicants, rotting toxicants, poisonous toxicants, asphyxiant toxicants, stimulant toxicants, and nerve toxicants. Nerve toxicants are the main type. Their function is to kill or to cause the loss of function. They are "distant brothers" of organic phosphorous farm chemicals, but their toxicity is far greater than that of such organic phosphorous farm chemicals.

The first nerve toxicant to appear was "tabun." It was discovered by fascist Germany in 1936 while studying organic phosphorous insecticides. It was followed in 1938 by the discovery of methyl O-isopropyl fluorophosphonic acid, commonly called "sarin." These two types of toxicants were not used in World War II because of strong protests by the world's peoples.

Nerve toxicants are generally liquid. When used, they are atomized or made into liquid droplets by explosion or other means. This type of poison gas will enter the human body when it is inhaled or when it comes into contact with the skin of a human being, and it will combine with acetyl cholinesterase in the human body, causing that enzyme to lose its activeness. Acetyl choline is the medium of transmission of nerve impulses at synapses. Under normal conditions, this medium is decomposed by acetyl cholinesterase within several milliseconds after it is released from the nerve endings. After this enzyme type loses its activeness, acetyl choline will accumulate, causing a series of symptoms of nerve poisoning, heavy sweating, congestion of the bronchi with phlegm, narrowing of the bronchi, blurred vision, vomiting and diarrhea, convulsion, and finally paralysis and cessation of breathing. The toxicant will cause death within several minutes. Poisoning by skin contact will cause death within several hours.

The nerve toxicants that have attracted the most attention besides sarin (also called GB) are methyl O-1, 2, 2-trimethyl propyl fluorophosphonic acid (also called GD or soman), and methyl O-ethyl S-2-di-isopropyl amino ethyl ester phosphonothiolic acid (also called VX). According to estimates, sarin's 50-percent lethal dosage in man is about 1 milligram, that of VX is 0.4 milligram, and that of soman is between the two. According to reports in foreign publications, sarin and VX are the two standard nerve gases of the United States, while soman is the standard nerve gas of the Soviet Union.

67

In March 1968, the United States military conducted a field experiment at (Dagewei). The nerve toxicant caused the death of 6,400 sheep and aroused domestic and foreign opposition. As a result, the United States spent 100 million dollars to sink most of its stockpile of chemical weapons into the sea. In 1973, an automatic filtering system for the nerve gas soman was discovered in Soviet-made tanks and armored transport vehicles captured in the Middle East war, attracting the attention of the U.S. military. Thus the U.S. Government began again to reorganize the chemical arsenal. To avoid causing strong opposition from public opinion, the military established a "binary weapons" development plan. The so-called binary weapon is a toxicant synthesized by two types of chemical substances. In peacetime, the two types of chemical substances are stored separately. But when they are detonated in a shell in time of war, the two types of chemicals will mix to form a deadly nerve gas. This is a new development in chemical weapons.

Other Members of Chemical Weapons Arsenal

Plant control chemicals such as the various toxicants that kill and defoliate plants are also a type of chemical weapon. The United States used 90,000 tons of this type of weapons in the 1960's in its aggressive war against Vietnam, and caused definite damage to the Vietnamese people. According to rumors, the West is secretly studying a kind of "antimaterials agent" that can damage military equipment and instruments so that they will malfunction. Belonging to this type are antilubricants and new catalysts.

Flamethrowing is another aspect of chemical warfare. This is a means of destroying blind angles and attacking by fire. During the Second World War, this [tactic] was widely used. According to foreign published reports, the Soviet Union has now refitted its T-55 tanks as flamethrowing tanks, using gel fuel to replace liquid fuel; the functional range is 100 meters. In combat, smokebombs and high-explosive shells are first used to confuse the enemy, after which the flamethrowing tanks approach the target and attack with flames. The U.S. military utilizes a kind of delayed action napalm bomb made of thickened triethyl aluminum.

That Zhugeliang borrowed the East Wind to attack the camp of Cao Chao by fire is a well-known story. This type of ancient flame attack and defense is still an important aspect of modern chemical warfare. The use of a wall of fire, scorching tactics, and arsonous mines to implement bombardment by flame have been seen more frequently in Soviet military exercises in recent years.

Smokescreens are another aspect of chemical warfare. They are often used as a means to defilade, to blind and confuse, to camouflage, and to communicate and avoid detection by infrared laser and microwave. U.S. experiments have shown that high temperatures (85°C or higher) can strengthen the defilading effect of different hygroscopic smokescreen materials such as red phosphorus, yellow phosphorus, and carbon trichloride. The new rifles produced by Sweden can shoot smoke bullets, using a mixture of titanium oxide and carbon trichloride. The maximum range of the bullet is 300 meters. After it is fired, it can produce a cloud of smoke 20 meters long and 4 meters wide. The U.S. Army will equip its M60A1 and M60A3 tanks with a smoke-generation system. Its smokescreen can effectively defilade visual and thermal image detection. It is predicted that smokescreens that can defilade large areas will emerge.

New Developments in Protective Clothing

The emergence of various chemical taxicants has also brought about more intensive research in protective clothing. There is a type of new carbon-containing, air-permeable, heat-radiating protective clothing made of two thin layers--one a mechanically strong and waterproof "outer layer" material, and the other an "inner layer" containing active carbon (or porous foam plastic). This is a kind of protective clothing that can protect against poison gas, can allow air to permeate, and is comfortable to wear. Because the material it uses is specially treated to become waterproof and oilproof, the active carbon can effectively absorb the vapors of toxicants and can protect against minute liquid droplets of the toxicants. The clothing is rainproof, fireproof, and washable. For example, the U.S. standard A gas mask and protective clothing and Britain's MK3 protective clothing belong to this type. New gas masks have eliminated the air hose, reduced resistance to air suction by 40 percent, expanded visibility by 30 percent, and are equipped with communicators. Britain has also designed an extra-large type of protective glasses so that children can recognize their mothers.

Some tanks and armored transport vehicles are equipped with automatic filtering systems for poison gas. The systems can filter out nerve toxicants such as soman. Some military equipment also has a layer of various types of special paint to prevent pollution from chemical warfare. For example, the United States already has 11 colors of polyamino formic ether camouflage and antipoison paint. Its use has basically solved the problem of disinfection of equipment polluted by poisons.

Each nation is engaged in the NBC three-in-one defense system. This is a defense system of the future against nuclear weapons, chemical weapons and biological weapons, a three-in-one system, because these three kinds of weapons can be defended against by a uniform type of protective clothing, by similar methods of protection, and by the same method to eliminate pollution.

According to revelations in Western publications, one flank of the Soviet troops along the Sino-Soviet border is equipped with nerve gas, mustard gas, and hydrogen cyanide. One flank of the Vietnamese troops along the Sino-Vietnamese border has chemical weapons. We must be on our guard.
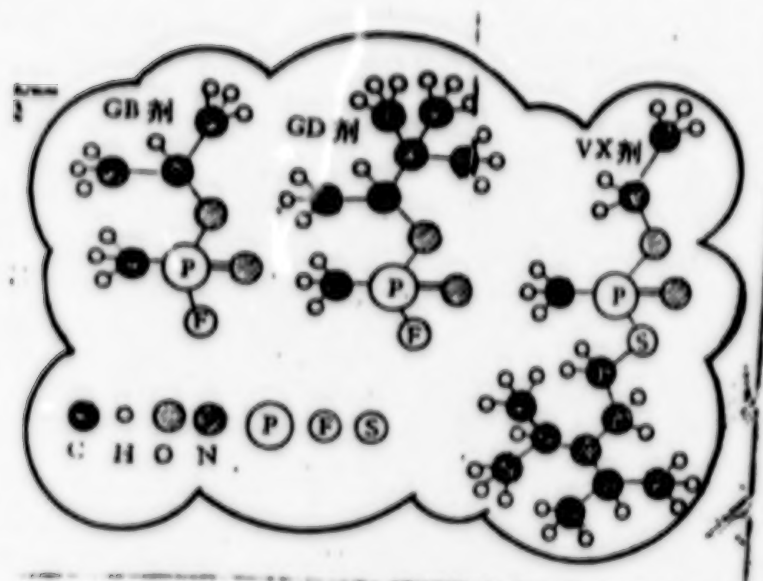
GB toxicant   GD toxicant   VX toxicant

END

END OF
FICHE
DATE FILMED

12 Aug. 1981